Accepted Manuscript

Structural, optical and vibrational properties of ZnO:M (M=Al^{3+} and Sr^{2+}) nano and micropowders grown by hydrothermal synthesis

Oscar Marin, Tania Soliz, Jorge Andrés Gutierrez, Mónica Tirado, Carlos Figueroa, David Comedi

PII: S0925-8388(19)30922-3

DOI: https://doi.org/10.1016/j.jallcom.2019.03.115

Reference: JALCOM 49879

To appear in: *Journal of Alloys and Compounds*

Received Date: 30 November 2018

Revised Date: 28 February 2019

Accepted Date: 6 March 2019

Please cite this article as: O. Marin, T. Soliz, Jorge.André. Gutierrez, Mó. Tirado, C. Figueroa, D. Comedi, Structural, optical and vibrational properties of ZnO:M (M=Al^{3+} and Sr^{2+}) nano and micropowders grown by hydrothermal synthesis, *Journal of Alloys and Compounds* (2019), doi: https://doi.org/10.1016/j.jallcom.2019.03.115.

Structural, optical and vibrational properties of ZnO:M (M=Al^{3+} and Sr^{2+}) nano and micropowders grown by hydrothermal synthesis

Oscar Marin[1,2,§], Tania Soliz[4], Jorge Andrés Gutierrez[5], Mónica Tirado[2,3], Carlos Figueroa[1,2] and David Comedi[1,2,*]

1. NanoProject y Laboratorio de Física del Sólido (LAFISO), Departamento de Física – Facultad de Ciencias Exactas y Tecnología, Universidad Nacional de Tucumán, Avenida Independencia 1800, San Miguel de Tucumán, Argentina.
2. Instituto de Física del Noroeste Argentino - INFINOA (CONICET-UNT), Tucumán, Argentina.
3. NanoProject y Laboratorio de Nanomateriales y Propiedades Dieléctricas (LNPD), Departamento de Física, Facultad de Ciencias Exactas y Tecnología, Universidad Nacional de Tucumán, Avenida Independencia 1800, San Miguel de Tucumán, Argentina.
4. Departamento de Ingeniería Biomédica, Facultad de Ciencias Exactas y Tecnología, Universidad Nacional de Tucumán, Avenida Independencia 1800, San Miguel de Tucumán, Argentina.
5. Facultad de Ciencias Básicas y Tecnologías, Universidad del Quindío, Armenia, Quindío, Colombia.

Abstract

Powders of ZnO and ZnO:M (M = Al^{3+} and Sr^{2+}) with 1 and 4% of M nominal content were synthetized by a hydrothermal method in a diethanolamine (DEA) medium. The samples were studied by scanning electron microscopy (SEM), X-ray diffraction (XRD), energy dispersive X-ray spectroscopy (EDX), micro-Raman and photoluminescence (PL). The powder particles were spherical with average radius decreasing from 1 μm down to 70 nm with increasing Al^{3+} nominal content but nearly independent on the Sr^{2+} nominal content. The XRD and micro-Raman results indicate that both Al^{3+} and Sr^{2+} mostly incorporated substitutionally into the ZnO lattice, giving rise to compressive and tensile strain, respectively, as a result of ionic radii differences. The PL spectra for ZnO:Al exhibit a dopant-induced contribution at ~3.1 eV, which is not observed for ZnO:Sr, due to radiative transitions involving trapping of photocarriers at theoretically expected substitutional Al^{3+} donor states or at Zn interstitial defects.

Keywords: *Hydrothermal synthesis; ZnO nano and microstructures; Diethanolamine; ZnO point defects; micro-Raman; Photoluminescence*.

Corresponding authors: §omarin@herrera.unt.edu.ar; *dcomedi@herrera.unt.edu.ar

1. Introduction

ZnO has been one of the most studied semiconductors during the last decade [1,2]. This continuing interest resides on the potential technological applications based on its unique properties, including direct wide-band gap in the UV range (3.37 eV), large exciton binding energy (60 meV), piezoelectricity, high surface reactivity, low toxicity, and many more. Some of its several applications are in gas sensing [3], biosensing [4], photocatalysis [5], optoelectronics [6], electronics [7], spintronics [8] and photonics [9]. Many of the proposed devices rely on the fact that ZnO can be easily and cost effectively nanostructured, giving rise to one of the richest families of semiconductor nanostructures known [10].

As with any semiconductor, many specific physical properties of ZnO thin films or nanostructures can be controlled and tailored according to the desired application through doping. In particular, various metal elements have been introduced into ZnO thin films and nanowires to increase magnetic moments [11], photocatalytical activities [12], electrical conductivity [13,14] or improve their biotechnological applications including human health treatments [15]. However, for any doping to be successful, the relation between the specific ZnO fabrication parameters and resulting physical properties must be known in as much detail as possible. This is because the properties of pure ZnO are themselves very sensitive to the crystal growth conditions and post-growth processing. For example, annealing treatments in oxygen rich atmospheres can change the photoluminescence of ZnO samples synthesized by sol-gel [16]; by using the vapor transport technique it is possible to control the morphology of ZnO nanostructures by changing the type of substrate and the ratio between oxygen pressure and local Zn partial pressure during growth [17]. A different way to improve physical

properties of ZnO is the formation of nanocomposites between ZnO and different materials, including compounds derived from carbon or mesoporous silica [18,19].

There have been many reports of doping of ZnO [14–16]. ZnO:Al (also known as AZO) is probably the most studied case mainly due to its convenient combination of high electrical conductivity and high optical transparency [24]. Recently, AZO was shown to be an interesting plasmonic material [25]. Regarding its luminescence properties, a blueshift of the ZnO UV emission band with Al doping has been observed and attributed to a bandgap increase related to the Burstein–Moss effect [26,27]. In addition, both Al-induced increment [28,29] and decrement [30,31] of the ZnO characteristic UV photoluminescence intensity have been reported. However, the mechanisms behind these behaviors and the reasons for the discrepancies have not been yet unveiled. In contrast to ZnO:Al, the ZnO:Sr system has been scarcely studied; nevertheless, due to the growing interest on the incorporation of alkaline earth metals onto the ZnO lattice, mainly for the improvement of ZnO nanostructures for photocatalysis and antibacterial applications [32,33], few reports on Sr incorporation effects on physical properties of ZnO have been published recently [34–36].

The solution-based syntheses are a good alternative to obtain ZnO and doped ZnO because they allow high control on the composition of synthesized materials, in addition to other advantages [37,38]. Among these techniques, the hydrothermal synthesis appears as an excellent and versatile option since, in addition to the good composition control, it is low cost, environmentally friendly, easily scalable and operates at relatively low temperatures [39,40]. Futhermore, the hydrothermal synthesis of ZnO nano and microstructured powders is a one-step and high yield process that offers good control of morphology [41–43].

In this work, we report the hydrothermal synthesis of ZnO, ZnO:Al and ZnO:Sr nano and microstructured powders at low temperature (125ºC) and focus mainly on their morphological, vibrational, structural and light emission properties. The powder particles are spherical with radii that are strongly reduced from ~1 μm down to 70 nm for Al additions but remain nearly unchanged for Sr additions. The Al is also seen to lead to a new emission component at ~3.1 eV, attributed to Zn interstitials. Both metal dopants incorporate mostly substitutionally into the ZnO lattice, leading to strains that affect the lattice parameter, phonon frequencies and UV emission spectra. These results should be valuable in the quest for new ZnO-based micro and nanostructures with new properties obtained by low-temperature fabrication routes.

2. Experimental section

The ZnO and ZnO:M (M = Al^{3+} and Sr^{2+}) samples were synthesized using distilled water, DEA, zinc nitrate dihydrate (0.5 M, aqueous solutions), strontium chloride hexahydrate and aluminum chloride hexahydrate (0.05 M, aqueous solutions) with Zn^{+2}, Sr^{+2} and Al^{+3} as precursors, respectively (Sigma-Aldrich, 99.99% purity, without further purification). Reactions were carried out in a 25 mL stainless steel autoclave with PTFE vessels. For this purpose, 1.5 mL of Zn^{+2} precursor solution, 3 mL of DEA, 0.15 mL or 0.6 mL of metal dopant solution (to obtain samples with 1% or 4% nominal dopant content, respectively), and distilled water (until completing 12.5 mL, i.e. 50% of autoclaves capacity) were added; then the autoclaves were closed and heated at 125 °C during 4 h. Finally, the autoclaves were cooled to room temperature. The powders obtained were isolated by centrifugation and washed with distilled water several times and dispersed in ethanol.

To obtain a sufficient amount of material for characterization, the powder dispersions were drop casted on square silicon substrates and dried at 125 °C. This procedure was repeated seven times. The morphology and particle size of the obtained solid samples were studied using scanning electron microscopy (SEM) (Carl-Zeiss model Supra 55-VP). The elemental composition was determined by energy-dispersive X-ray spectroscopy (EDX). The crystalline structure was studied with X-ray diffraction (XRD) [SIEMENS D5000 diffractometer with Cu Kα radiation source (1.54056 Å)]; patterns were recorded in the 30-60° range. Micro-Raman measurements were carried out using a 532 nm wavelength, 10 mW power laser (DXR Smart Raman Spectrometer, Thermo Scientific). PL spectra were obtained using backscattering geometry, with a 15 mW He-Cd laser set at a wavelength of 325 nm as excitation source; light emitted from the samples was focalized on a CCD spectrometer with two biconvex lenses. A filter was placed at the entrance of the spectrometer to eliminate scattered laser radiation.

3. Results and discussion

Fig. 1(a-g) show SEM micrographs of the synthesized ZnO, ZnO:Al, ZnO:Sr powders. As it can be seen, all samples are composed of particles with a spherical morphology, independently of the metal constituent (Zn^{2+}, Al^{3+} or Sr^{2+}). This morphology seems to be a consequence of particle agglomeration in the solution during hydrothermal growth. Indeed, this result is in agreement with previous reports where the hydrothermal synthesis of ZnO using DEA was observed to lead to powders composed of spheres with similar characteristics [41,44]. This particular morphology is consequence of the addition of DEA in the hydrothermal synthesis, which causes, in a first stage, the formation of ZnO nanoparticles and, in a final stage, their agglomeration [41]. However, although the spherical shape is not very affected by the addition of Al^{3+}

or Sr^{2+} cations, the average size (and size dispersion) of the spheres, especially for Al^{3+} additions, are significantly changed. The average microsphere sizes were determined from SEM images using ImageJ open source software processing. For this purpose, the grains were identified and their size measured from the SEM images; average sizes were calculated and their values were rounded up in consistency with the expected accuracy of the SEM instrument. According to the above, the average particle sizes were 1.1 μm, 1 μm and 1.5 μm for ZnO, ZnO:Sr 1% and ZnO:Sr 4 % respectively, while for ZnO:Al they were drastically reduced (150 nm and 70 nm for ZnO:Al 1% and 4%, respectively). Since the synthesis was performed with the same experimental parameters (temperature, volume, solvents and precursors concentrations), it is evident that the size of the particles is strongly affected by the addition of Al^{3+} cations.

The EDX elemental composition analysis for all samples is presented in Fig. 2(a-e). The presence of both Al and Sr in the corresponding samples is confirmed and, as will be discussed later, both metals are effectively incorporated to the ZnO lattice. In all EDX spectra, a Si peak from the Si substrate is also detected.

The XRD patterns from the samples acquired between 30º and 60º 2θ are presented in Fig. 3. As noted, all the samples have a polycrystalline structure; patterns show the (100), (002), (101), (102) and (110) peaks corresponding to the wurtzite crystalline structure of ZnO according to the JCPDS 036-1451 card. In addition, no secondary phases of strontium oxides or aluminum oxides are detected.

Lattice parameters were found by using the FullProf software in the pattern matching mode (Le Bail refinement) [45] and the results are summarized in Table 1. As observed, for the pure ZnO sample, the *c* and *a* parameters found have values of 5.2041 and 3.2491 nm, respectively. Furthermore, both parameters decrease with increasing Al^{3+} nominal content in ZnO:Al and increase with increasing Sr^{2+} nominal content in

ZnO:Sr. The lattice parameter changes can be explained by differences in ionic radii between the cations involved: Al^{3+} (0.053 nm) < Zn^{2+} (0.074 nm) < Sr^{2+} (0.118 nm) [46]. Given that the ionic radius of Zn^{2+} is greater than that of Al^{3+} and lower than that of Sr^{2+}, the values of the lattice parameters found suggest that the dopant metals are substitutionally incorporated into the ZnO lattice.

Crystallite sizes, stress and strain were estimated through the Williamson-Hall (WH) analysis, using the Uniform Stress Deformation Model (USDM), taking into account the following assumptions: (i) crystals have a homogeneous isotropic nature, so that the lattice deformation is uniform and (ii) the stress in the spheres is sufficiently low, so that the linear proportionality relation between stress (σ) and strain (ε) given by $\sigma = E\varepsilon$, where *E* is Young's modulus [47,48], holds. Combining the Scherrer equation $D = K\lambda/(\beta_{hkl}cos\theta)$ with the strain-induced broadening arising from crystal imperfections and distortion $\varepsilon \approx \beta_{hkl}/tan\theta$ and σ [47,48], the following USDM equation is deduced:

$$\beta_{hkl}cos\theta = \frac{K\lambda}{D} + \frac{4\sigma sin\theta}{E_{hkl}} \quad (1);$$

where β_{hkl} is the peak FWHM, θ is the peak position, *K* is a constant with a value of 0.94, λ is the X-ray wavelength (0.15406 nm), *D* is the crystallite size and E_{hkl} is the Young's modulus in the direction normal to the (*hkl*) planes. For a hexagonal crystal, Young's modulus is given by the following relation:

$$E_{hkl} = \frac{\left[h^2+\frac{(h+2k)^2}{3}+\left(\frac{al}{c}\right)^2\right]^2}{s_{11}\left(h^2+\frac{(h+2k)^2}{3}\right)^2+s_{33}\left(\frac{al}{c}\right)^4+(2s_{13}+s_{44})\left(h^2+\frac{(h+2k)^2}{3}\right)\left(\frac{al}{c}\right)^2} \quad (2);$$

Where s_{11}, s_{13}, s_{33}, s_{44} are the elastic compliances of ZnO, whose values are 7.858 x 10^{-12}, -2.206 x 10^{-12}, 6.940 x 10^{-12}, 23.57 x 10^{-12} m^2 N^{-1}, respectively [49]. The USDM plots are presented in Fig. 4; the corresponding crystallite size, stress and strain values are summarized in Table 1. As can be seen, Al doping reduces the lattice parameters and produces compressive stress, while Sr doping increases the lattice parameters and produces tensile stress.

Considering the crystallite size estimated by the WH analysis and recalling the discussion about the particles size determined by SEM, it is clear that incorporation of Al^{3+} in ZnO has a stronger effect on particle size than on crystallite size (note that each particle contains several crystallites and this is why particle sizes as determined from SEM are always larger than crystallite sizes as determined by XRD). This suggests that the origin of particle size reduction induced by Al^{3+} incorporation is not related to factors pertaining crystal growth (e.g. nucleation growth rate), which would primarily affect the crystallite size. The DEA is involved in multiples stages in the hydrothermal synthesis of ZnO, including (i) chelating the Zn^{2+} (M^{n+}) cations by the formation of DEA – Zn – O – Zn – DEA chains (forming a stable colloidal phase), (ii) providing a growth medium at basic pH, (iii) controlling the morphology by the coordination to specific crystal faces and (iv) promoting nanoparticle agglomeration [41]. Although the microscopic chelation mechanism is still poorly understood, it is clear that addition of Al^{3+} modifies the DEA – Zn – O – Zn – DEA chain formation process and interferes with nanoparticle aggregation, inhibiting the formation of large spheres.

Table 1 Crystalline data obtained from diffraction pattern.

Sample	a (Å)	c (Å)	D (nm)	σ (MPa)
ZnO	3.2491	5.2041	28	60.1
ZnO:Al 1%	3.2433	5.1965	29	-28.5
ZnO:Al 4%	3.2399	5.1871	27	-12.6
ZnO:Sr 1%	3.2492	5.2044	40	75.1
ZnO:Sr 4%	3.2565	5.2198	48	140.6

In addition, the lattice parameter changes suggest that there are differences in the nature of strain for the different incorporated cations into the ZnO lattice: Since both the *c* and *a* parameters become shorter with increasing Al^{3+} nominal content, the ZnO lattice is under compressive strain; in contrast, inclusion of Sr^{2+} causes tensile strain [50]. This result is confirmed by the WH analysis, since the positive slope in the Fig. 4(a, c, d) indicates effectively that there is tensile strain for the ZnO and ZnO:Sr samples, while the negative slope for ZnO:Al samples indicates that strain is compressive [51].

In order to study the effects of Al^{3+} and Sr^{2+} incorporation on the vibrational properties of ZnO, we measured the micro-Raman spectra for all samples at room temperature in the 70 to 500 cm^{-1} frequency range; results are presented in Fig. 5. As it is well known, group theory predicts the following Raman active modes for ZnO: $A_1 + 2E_2 + E_1$, where A_1 and E_1 are polar modes exhibiting two different frequencies for transverse optical (TO) and longitudinal optical (LO) phonons: $A_1(TO)$, $A_1(LO)$, $E_1(TO)$ and $E_1(LO)$, at about 379, 574, 410 and 591 cm^{-1}, respectively. The E_2 modes, in turn, are nonpolar, appearing at about 102 cm^{-1} (E_2^{low}) and 439 cm^{-1} (E_2^{high}), being associated with vibration of zinc and oxygen sublattices, respectively [52,53]. As it is observed, our spectra are dominated by both E_2 modes, which are the most prominent peaks for the wurtzite structure [54]. The A_1(TO) and E_1(TO) modes can also be identified in the spectra. In addition, a second order peak associated to E_2^{high} - E_2^{low} appears close to 330 cm^{-1} [53].

Both E_2 modes observed in Fig. 5 were fitted with the Breit-Wigner (BW) function:

$$I(\omega) \propto \frac{[1+2\beta(\omega-\omega_0)/\Gamma]^2}{1+[2(\omega-\omega_0)/\Gamma]^2} \qquad (3);$$

where $I(\omega)$ is the Raman intensity, ω_0 is the Raman shift, Γ is the FWHM, and β is an asymmetry parameter ($\beta = 0$ for a symmetrical peak) [55,56]. Although, the BW function has been usually used to analyze Raman spectra of carbon-based materials, it has been also applied for the analysis of Raman spectra from $Zn_xMg_{1-x}O$, yttria-stabilized zirconia and $CuAlO_2$ nanoparticles [55–57]. The fits of the experimental data for both E_2^{low} and E_2^{high} modes are shown in Figures 6 and 7. It is clear that the BW function fits the experimental data satisfactorily.

The set of ω_0, Γ and β values determined from the fits are summarized in Table 2. As can be observed in the Table, the lineshape parameters Γ and β do not change systematically with the Al or Sr nominal content. Linewidth broadening of Raman peaks in ZnO upon doping has been observed and attributed to disorder effects resulting in translational symmetry disruption of the wurtzite lattice due to dopant incorporation [55,58]. In our case, the observed linewidth changes induced by Al^{3+} or Sr^{2+} are relatively small, indicating relatively small disorder introduced by these metal ions for the nominal concentrations used (1 and 4%).

The ω_0 values for both E_2^{low} and E_2^{high} modes are depicted in Fig. 6(f) and Fig. 7(f) against the nominal Al and Sr contents. As can be noted, ω_0 for both the E_2^{low} and E_2^{high} modes increase with Al^{3+} nominal content and both decrease with Sr^{2+} nominal content. Since the shifts of ω_0 occur in the same direction for both E_2^{low} and E_2^{high} modes for each dopant, we believe these shifts must have a common origin. Indeed, both modes result from atomic vibrations perpendicular to the *c* axis of wurtzite. Furthermore, the force constants associated with both modes are both related to some component of the Zn – O bonds connecting the Zn and O sublattices. Hence, it may be

expected that force constant changes induced by a certain metal dopant should affect both the E_2^{low} and E_2^{high} modes frequencies in a similar fashion. However, considering the well-known relation for the oscillator frequency:

$$\omega_0 = \frac{1}{2\pi}\sqrt{\frac{k}{\mu}} \quad (4);$$

where k is the force constant and μ is the reduced mass, it is clear that doping-induced changes in μ must also be considered. It is well known that the E_2^{low} mode in ZnO, which involves primarily (i.e. 85%) displacement of the cation (Zn^{2+}) sublattice, is therefore sensitive to changes in the cation effective mass due to doping as Zn^{2+} are replaced by the dopant ions. In contrast, the E_2^{high} mode, which involves primarily displacement of the anion (O^{2-}) sublattice, does not change much in response to modifications in the effective cationic mass. Hence, other origins have been invoked to explain doping induced changes in the E_2^{high} frequency, such as lattice parameter and associated force constant changes [55,59].

In our case, however, it is clear that the replacement of Zn^{2+} by Al^{3+} leads to a reduction of the lattice parameters due to the lower ionic radius of Al^{3+}. This in general leads to an increase of k and therefore should contribute to increases of both, the E_2^{low} and E_2^{high} modes frequencies with increasing Al nominal content in ZnO:Al. Indeed, this is the case from the experimental side [see left hand side of Fig. 6(f) and 7(f)]. The opposite should occur when replacing Zn^{2+} by Sr^{2+} due to the larger Sr^{2+} radius, and hence both the E_2^{low} and E_2^{high} frequencies should decrease with increasing Sr nominal content in ZnO:Sr, as observed in the Raman measurement [see right hand side of Fig. 6(f) and 7(f)].

For the E_2^{low} mode, however, taking into account the differences in atomic mass between Zn^{2+} (65.38 u), Al^{3+} (26.98 u) and Sr^{2+} (87.62 u), the incorporation of Al^{3+} at the expense of Zn^{2+} should also contribute to an increase in the phonon frequency as

consequence of an effective cationic mass reduction [55,60]. This in principle should also apply to the Sr^{2+} case, but contributing to an increase of the effective mass and a lowering in the phonon frequency. These results are compatible with Figures 6(f) and 7(f) and support the hypothesis that both Al^{3+} and Sr^{2+} are being incorporated substitutionally into the ZnO lattice (specifically, into the Zn^{2+} sublattice), as previously suggested by the XRD analysis.

Other contributions, especially to the E_2^{high} mode frequency, could come from the presence of internal strains [61–63], which seem to be unimportant here. In addition, it has been reported for interstitial dopants in ZnO that the E_2^{high} mode intensity is strongly reduced due to the breakdown of translational crystal symmetry [64]. As observed in Fig. 7(a-d), the intensity of this mode does not have important changes with the additions of Al^{3+} or Sr^{2+} in our samples. This, again, indicates that the incorporation of these metals into the ZnO lattice occurs mainly substitutionally and hence does not result in strong crystal distortions, as previously suggested by the relatively small Raman peak linewidth changes observed.

Table 2. Parameters obtained from the fit of Eq. 3 to the Raman E_2^{low} and E_2^{high} peaks observed from the synthesized samples.

Sample	E_2^{low}	Γ (E_2^{low})	β (E_2^{low})	E_2^{high} - E_2^{low}	E_2^{high}	Γ (E_2^{high})	β (E_2^{high})
ZnO	98.6	3.57	-6.35	331.4	438.6	6.61	-5.45
ZnO:Al 1%	98.8	3.75	-5.34	331.9	438.7	6.53	-5.93
ZnO:Al 4%	99.1	3.68	-2.53	331.9	438.9	6.58	-5.53
ZnO:Sr 1%	98.3	3.42	-7.26	330.9	438.2	6.19	-4.69
ZnO:Sr 4%	97.9	3.54	-7.62	331.9	438.1	6.83	-5.08

In Fig. 8(a,b), the PL spectra for the ZnO:Al and ZnO:Sr samples are shown (in both figures, they are compared to the PL spectrum for the ZnO sample). For pristine ZnO, a peak due to excitonic radiative recombinations in the UV at 385 nm (3.221 eV) and a band in the visible peaked at ~570 nm (2.175 eV) due to deep defect states, are observed. As noted in Fig. 8(a), the incorporation of Al^{3+} into the ZnO lattice leads to a

quenching of both UV and visible emissions, while incorporation of Sr^{2+} does not lead to a clear tendency, as seen in Fig. 8(b). The PL intensity reduction for ZnO:Al samples [Fig. 8(a)] may suggest that Al^{3+} behaves as a non-radiative recombination center, competing with radiative recombination processes and leading to the PL quenching in function of Al^{3+} nominal content. In Fig. 8(c,d), the normalized emission bands in the UV and visible regions of the spectrum are shown. As depicted in Fig. 8(d), the shape of the visible emission band peaked at ~570 nm, which has been attributed to oxygen vacancies (V_O) [16,41], does not change with Al^{3+} and Sr^{2+} incorporation. Hence it can be concluded that additions of both Al^{3+} and Sr^{2+} to the ZnO lattice do not induce additional luminescent defect centers.

Regarding the mechanisms behind the UV emission (related to band-to-band recombination and recombination processes involving near band edge states), the effects of Al^{3+} incorporation are noticeable: the UV band is blue-shifted and broadened with respect that of ZnO sample [Fig. 8(c)]. These blue-shifts could be due to the Burstein–Moss effect [26,27] or related to bandgap widening associated with the compressive strains deduced from the XRD and Raman measurements. The effects of the Sr^{2+}incorporation, in contrast, are less noticeable. In order to study the nature of the UV emission, we decompose the PL spectra in the UV region to its assumed Gaussian components. The results are shown in Fig. 9 and summarized in Table 3. As it can be noted, the spectra from ZnO and ZnO:Sr [Figures 9(a), (d) and (e)] could be satisfactorily fit with 2 components only. From inspection of Table 3, it is deduced that both components in ZnO:Sr are slightly red-shifted with respect to those in ZnO and that the redshift increases as function of the Sr^{2+} nominal content. The red-shifts could be related to small bandgap narrowing associated with the tensile strains deduced from XRD and Raman. In addition, the energy differences between the two UV components

are 61, 70 and 71 meV for ZnO, ZnO:Sr 1% and ZnO:Sr 4%, respectively, which are close to the ZnO LO phonon energy ($\hbar\omega_{LO} \approx 71\ meV$) [23]. Hence, it is reasonable to assume that these components correspond to the first (FX-1LO) and the second (FX-2LO) exciton phonon replicas, which usually dominate the UV emission band from ZnO at room temperature [65].

In contrast, a third component, centered at about 400 nm (~3.1 eV), appears for ZnO:Al. Furthermore, as mentioned above (Table 3), the first two components are blue-shifted with respect to those for the undoped ZnO sample. Since the energy differences between the two first components are 67 and 77 eV for ZnO:Al 1% and ZnO:Al 4%, respectively, their origin can also be related to the FX-1LO and FX-2LO phonon replicas. Regarding the third component at ~3.1 eV, the energy differences with respect the FX-2LO component (105 and 116 eV for 1% and 4% of Al^{3+} nominal content, respectively) are significantly larger than the ZnO phonon energy, indicating that it is not an additional phonon replica. Indeed, we notice that a component at ~3.1 eV has been observed before in Al-doped ZnO and attributed to near-edge states associated with Al substitution of Zn [66]. Shallow donor states due to due to Al 3s electrons from substitutional Al in ZnO are predicted by density functional theory based calculations [67]. As a matter of fact, for sufficiently large Al concentration, some of these states are responsible for the well-known semi-metallic character of electrical transport in ZnO:Al. It is possible that the shoulders observed at 400 nm (i.e. 3.1 eV) in the PL spectra for both Al-doped ZnO samples in Fig. 8(c) are due to radiative transitions involving Al-induced donor states. However, we note that a PL contribution at about 3.1 eV has been also reported for undoped ZnO and attributed to Zn interstitials (Zn_i) [68]. It is not clear at this stage why formation of Zn_i would be favored in ZnO:Al samples grown by hydrothermal synthesis. It is interesting to note that Zn_i is a relatively unstable

point defect due to a low diffusion barrier [69, 70] that can be stabilized by the interaction with V_O [71]. Hence, we speculate that at some growth stage, the incorporation of Al^{3+} in substitutional way could help to stabilize the Zn_i. Note, however, that this effect is not observed for ZnO:Sr.

Table 3. Parameters extracted from Gaussian function fits to the UV emissions

Sample	FX-1LO (eV)	FX-2LO (eV)	~3.1eV peak (eV)	(FX-1LO) – (FX-2LO) (meV)	(FX-2LO) – ~3.1eV peak (meV)
ZnO	3.236	3.175	-	61	-
ZnO:Al 1%	3.271	3.204	3.099	67	105
ZnO:Al 4%	3.297	3.220	3.104	77	116
ZnO:Sr 1%	3.235	3.165	-	70	-
ZnO:Sr 4%	3.222	3.151	-	71	-

4. Conclusions

Powders composed by nano and microspheres of ZnO and ZnO:M with M = Al^{3+} and Sr^{2+} were obtained through hydrothermal route using diethanolamine. XRD and micro-Raman results indicate that both Al^{3+} and Sr^{2+} are mainly incorporated into ZnO substitutionally. All samples exhibit wurtzite structure and spherical morphology. A large reduction on the average sphere size with increasing Al^{3+} nominal content was observed, indicating that the Al^{3+} interacts with diethanolamine in a way to inhibit its function as an aggregation agent, preventing the formation of large spheres. From the crystallite sizes and strains estimated by means of Williamson-Hall analysis of the observed XRD patterns using the Uniform Stress Deformation Model (USDM), it was found that incorporation of Al^{3+} into the ZnO lattice induces compressive strain while Sr^{2+} induces tensile strain. These effects are consistent with the phonon frequency shifts observed by Raman spectroscopy [Figures 6 and 7(f)] and are expected from differences between the ionic radii of substitutional cations (0.053 nm for Al^{3+} and 0.118 nm for Sr^{2+}) and that of the host Zn^{2+} (0.074 nm). The effects of Al^{3+} and Sr^{2+} additions on the

PL spectra were also studied. The most remarkable observation was a new component to the UV band at ~3.1 eV for ZnO:Al, not observed for ZnO:Sr, attributed to substitutional Al^{3+} donor states or to the Zn interstitial defect. The exact nature of this component for Al^{3+} incorporation in ZnO should be matter of further research.

Acknowledgments

We are grateful for financial funding by the Secretaría de Ciencia, Arte e Innovación Tecnológica (SCAIT) of the Universidad Nacional de Tucumán (PIUNT E637 and CIUNT 26/E439); the Argentinean agencies CONICET (PIP 411) and ANPCyT (FONCyT – BID PICT 2015-0865). JAG thanks to Dr. Cristian Villa, Instituto Interdisciplinario de las Ciencias and Universidad del Quindío.

References

[1] L. Schlur, J.R. Calado, D. Spitzer, Synthesis of zinc oxide nanorods or nanotubes on one side of a microcantilever, R. Soc. Open Sci. 5 (2018) 1–11. doi:10.1098/rsos.180510.

[2] L.R. Valério, N.C. Mamani, A.O. De Zevallos, A. Mesquita, M.I.B. Bernardi, A.C. Doriguetto, H.B. De Carvalho, Preparation and structural-optical characterization of dip-coated nanostructured Co-doped ZnO dilute magnetic oxide thin films, RSC Adv. 7 (2017) 20611–20619. doi:10.1039/c7ra01200d.

[3] L. Zhu, W. Zeng, Room-temperature gas sensing of ZnO-based gas sensor: A review, Sensors Actuators, A Phys. 267 (2017) 242–261. doi:10.1016/j.sna.2017.10.021.

[4] P. Gallay, E. Tosi, R. Madrid, M. Tirado, D. Comedi, Glucose biosensor based on functionalized ZnO nanowire / graphite fi lms dispersed on a Pt electrode, Nanotechnology. 27 (2016) 425501. doi:10.1088/0957-4484/27/42/425501.

[5] S. Bhatia, N. Verma, Photocatalytic activity of ZnO nanoparticles with optimization of defects, Mater. Res. Bull. 95 (2017) 468–476. doi:10.1016/j.materresbull.2017.08.019.

[6] E. Muchuweni, T.S. Sathiaraj, H. Nyakotyo, Synthesis and characterization of zinc oxide thin films for optoelectronic applications, Heliyon. 3 (2017) e00285. doi:10.1016/j.heliyon.2017.e00285.

[7] H. Shin, C.M. Kang, K.H. Baek, J.Y. Kim, L.M. Do, C. Lee, Low-temperature solution-processed zinc oxide field effect transistor by blending zinc hydroxide and zinc oxide nanoparticle in aqueous solutions, Jpn. J. Appl. Phys. 57 (2018) 05GD04. doi:10.7567/JJAP.57.05GD04.

[8] R. Elilarassi, G. Chandrasekaran, Optical, electrical and ferromagnetic studies of

ZnO:Fe diluted magnetic semiconductor nanoparticles for spintronic applications, Spectrochim. Acta - Part A Mol. Biomol. Spectrosc. 186 (2017) 120–131. doi:10.1016/j.saa.2017.05.065.

[9] A. Anopchenko, S. Gurung, L. Tao, C. Arndt, H.W.H. Lee, Atomic layer deposition of ultra-thin and smooth Al-doped ZnO for zero-index photonics, Mater. Res. Express. 5 (2018) 014012. doi:10.1088/2053-1591/aaa653.

[10] Z.L. Wang, Nanostructures of zinc oxide, Mater. Today. 7 (2004) 26–33. doi:10.1016/S1369-7021(04)00286-X.

[11] M. Shatnawi, A.M. Alsmadi, I. Bsoul, B. Salameh, G.A. Alna'washi, F. Al-Dweri, F. El Akkad, Magnetic and optical properties of Co-doped ZnO nanocrystalline particles, J. Alloy. Compd. J. 655 (2016) 244–252. doi:10.1016/j.jallcom.2015.09.166.

[12] R. Saleh, N.F. Djaja, Transition-metal-doped ZnO nanoparticles: Synthesis, characterization and photocatalytic activity under UV light, Spectrochim. Acta - Part A Mol. Biomol. Spectrosc. 130 (2014) 581–590. doi:10.1016/j.saa.2014.03.089.

[13] H. Hagendorfer, K. Lienau, S. Nishiwaki, C.M. Fella, L. Kranz, A.R. Uhl, D. Jaeger, L. Luo, C. Gretener, S. Buecheler, Y.E. Romanyuk, A.N. Tiwari, Highly transparent and conductive ZnO: Al thin films from a low temperature aqueous solution approach, Adv. Mater. 26 (2014) 632–636. doi:10.1002/adma.201303186.

[14] E. Manikandan, V. Murugan, G. Kavitha, P. Babu, M. Maaza, Nano flower rod wire-like structures of dual metal (Al and Cr) doped ZnO thin films: Structural , optical and electronic properties, Mater. Lett. 131 (2014) 225–228. doi:10.1016/j.matlet.2014.06.008.

[15] A. Manikandan, E. Manikandan, B. Meenatchi, S. Vadivel, S.K. Jaganathan, R. Ladchumananandasivam, M. Henini, M. Maaza, J.S. Aanand, Rare earth element (REE) lanthanum doped zinc oxide (La: ZnO) nanomaterials: Synthesis structural optical and antibacterial studies, J. Alloys Compd. 723 (2017) 1155–1161. doi:https://doi.org/10.1016/j.jallcom.2017.06.336.

[16] O. Marin, M. Tirado, N. Budini, E. Mosquera, C. Figueroa, D. Comedi, Photoluminescence from c-axis oriented ZnO films synthesized by sol-gel with diethanolamine as chelating agent, Mater. Sci. Semicond. Process. 56 (2016) 59–65. doi:10.1016/j.mssp.2016.07.007.

[17] G. Grinblat, M.G. Capeluto, M. Tirado, A. V. Bragas, D. Comedi, Hierarchical ZnO nanostructures : Growth mechanisms and surface correlated photoluminescence, Appl. Phys. Lett. 100 (2012) 233116. doi:10.1063/1.4724195.

[18] B. Sathyaseelan, E. Manikandan, K. Sivakumar, J. Kennedy, M. Maaza, Enhanced visible photoluminescent and structural properties of ZnO / KIT-6 nanoporous materials for white light emitting diode (w-LED) application, J. Alloys Compd. 651 (2015) 479–482.

[19] E. Manikandan, G. Kavitha, J. Kennedy, Epitaxial zinc oxide , graphene oxide composite thin films by laser technique for micro-Raman and enhanced field emission study, Ceram. Int. 40 (2014) 16065–16070. doi:10.1016/j.ceramint.2014.07.129.

[20] H.J. Fan, Y. Yang, M. Zacharias, ZnO-based ternary compound nanotubes and nanowires, J. Mater. Chem. 19 (2009) 885–900. doi:10.1039/b812619d.

[21] J. Ghosh, R. Ghosh, P.K. Giri, Chemical Tuning the visible photoluminescence in Al doped ZnO thin film and its application in label-free glucose detection,

Sensors Actuators B. Chem. 254 (2018) 681–689. doi:10.1016/j.snb.2017.07.110.
[22] H. Yin, J. Chen, Y. Wang, J. Wang, H. Guo, Composition dependent band offsets of ZnO and its ternary alloys, Nat. Publ. Gr. (2017) 1–7. doi:10.1038/srep41567.
[23] O. Marin, P. Alastuey, E. Tosi, J. Orive, E. Mosquera, G. Zampieri, S. Suárez, D. Comedi, M. Tirado, Suppression of the green emission, texturing , solute-atom di ff usion and increased electron-phonon coupling induced by Ni in sol-gel ZnNiO thin films, Appl. Surf. Sci. 456 (2018) 771–780. doi:10.1016/j.apsusc.2018.06.169.
[24] B.K. Sharma, N. Khare, Stress-dependent band gap shift and quenching of defects in Al-doped ZnO films, J. Phys. D. Appl. Phys. 43 (2010) 465402. doi:10.1088/0022-3727/43/46/465402.
[25] A.K. Pradhan, R.M. Mundle, K. Santiago, J.R. Skuza, B. Xiao, K.D. Song, M. Bahoura, R. Cheaito, P.E. Hopkins, Extreme tunability in aluminum doped Zinc Oxide plasmonic materials for near-infrared applications, Sci. Rep. 4 (2014) 19–21. doi:10.1038/srep06415.
[26] X. Zi-qiang, D. Hong, L. Yan, C. Hang, Al-doping effects on structure, electrical and optical properties of c-axis-orientated ZnO:Al thin films, Mater. Sci. Semicond. Process. 9 (2006) 132–135. doi:10.1016/j.mssp.2006.01.082.
[27] M. Wang, K.E. Lee, S.H. Hahn, E.J. Kim, S. Kim, J.S. Chung, E.W. Shin, C. Park, Optical and photoluminescent properties of sol-gel Al-doped ZnO thin films, Mater. Lett. 61 (2007) 1118–1121. doi:10.1016/j.matlet.2006.06.065.
[28] W. Wang, T. Ai, W. Li, R. Jing, Y. Fei, X. Feng, Photoelectric and Electrochemical Performance of Al-Doped ZnO Thin Films Hydrothermally Grown on Graphene-Coated Polyethylene Terephthalate Bilayer Flexible Substrates, J. Phys. Chem. C. 121 (2017) 28148–28157. doi:10.1021/acs.jpcc.7b08181.
[29] M.C. Jun, S.U. Park, J.H. Koh, Comparative studies of Al-doped ZnO and Gadoped ZnO transparent conducting oxide thin films, Nanoscale Res. Lett. 7 (2012) 1–6. doi:10.1186/1556-276X-7-639.
[30] M. Ahmad, E. Ahmed, Y. Zhang, N.R. Khalid, J. Xu, M. Ullah, Z. Hong, Preparation of highly efficient Al-doped ZnO photocatalyst by combustion synthesis, Curr. Appl. Phys. 13 (2013) 697–704. doi:10.1016/j.cap.2012.11.008.
[31] Y. Liu, J. Lian, Optical and electrical properties of aluminum-doped ZnO thin films grown by pulsed laser deposition, Appl. Surf. Sci. 253 (2007) 3727–3730. doi:10.1016/j.apsusc.2006.08.012.
[32] L. El Mir, Luminescence properties of calcium doped zinc oxide nanoparticles, J. Lumin. 186 (2017) 98–102.
[33] A.S.H. Hameed, C. Karthkeyan, S. Sasikumar, V.S. Kumar, S. Kumaresan, G. Ravi, Impact of alkaline metal ions Mg2+, Ca2+, Sr2+ and Ba2+ on the structural, optical, thermal and antibacterial properties of ZnO nanoparticles prepared by the co-precipitation metho..., J. Mater. Chem. B. 1 (2013) 5950. doi:10.1039/C3TB21068E.
[34] A. Kumar, R. Das, Y. Kumar, S. Sen, P.M. Shirage, Applied Surface Science Growth of transparent Zn 1 − x Sr x O (0 . 0 ≤ x ≤ 0 . 08) films by facile wet chemical method : Effect of Sr doping on the structural , optical and sensing properties, Appl. Surf. Sci. 379 (2016) 23–32.
[35] K.P. Raj, K. Sadaiyandi, A. Kennedy, R. Thamizselvi, Structural , optical , photoluminescence and photocatalytic assessment of Sr-doped ZnO nanoparticles, Mater. Chem. Phys. 183 (2016) 24–36.
[36] P. V Raghavendra, J.S. Bhat, N.G. Deshpande, Enhancement of

photoluminescence in Sr doped ZnO thin fi lms prepared by spray pyrolysis, Mater. Sci. Semicond. Process. 68 (2017) 262–269.
[37] M. Cargnello, T.R. Gordon, C.B. Murray, Solution-phase synthesis of titanium dioxide nanoparticles and nanocrystals, Chem. Rev. 114 (2014) 9319–9345. doi:10.1021/cr500170p.
[38] Y. Jianfeng, Q. Limin, Solution-phase synthesis of one-dimensional semiconductor nanostructures, J. Mater. Sci. Technol. 24 (2008) 529–540. doi:10.1109/IEMBS.2005.1616451.
[39] S. Baruah, J. Dutta, Hydrothermal growth of ZnO nanostructures, Sci. Technol. Adv. Mater. 10 (2009) 013001. doi:10.1088/1468-6996/10/1/013001.
[40] M. Shandilya, R. Rai, J. Singh, Review: Hydrothermal technology for smart materials, Adv. Appl. Ceram. 115 (2016) 354–376. doi:10.1080/17436753.2016.1157131.
[41] V. González, O. Marin, M. Tirado, D. Comedi, Metastability effects on the photoluminescence of ZnO nano-micro structures grown at low temperature and influence of the precursors on their morphology and structure, Mater. Res. Express. 5 (2018) 125003. doi:10.1088/2053-1591/aadfc4.
[42] J. Joo, B.Y. Chow, M. Prakash, E.S. Boyden, J.M. Jacobson, Face-selective electrostatic control of hydrothermal zinc oxide nanowire synthesis, Nat. Mater. 10 (2011) 596–601. doi:10.1038/nmat3069.
[43] R. Boppella, K. Anjaneyulu, P. Basak, S. V. Manorama, Facile synthesis of face oriented ZnO crystals: Tunable polar facets and shape induced enhanced photocatalytic performance, J. Phys. Chem. C. 117 (2013) 4597–4605. doi:10.1021/jp311443s.
[44] R. Razali, A.K. Zak, W.H.A. Majid, M. Darroudi, Solvothermal synthesis of microsphere ZnO nanostructures in DEA media, Ceram. Int. 37 (2011) 3657–3663. doi:10.1016/j.ceramint.2011.06.026.
[45] J. Rodríguez-Carvajal, Recent advances in magnetic structure determination by neutron powder diffraction, Phys. B Condens. Matter. 192 (1993) 55–69. doi:10.1016/0921-4526(93)90108-I.
[46] M.G. Brik, A. Suchocki, A. Kamińska, Lattice parameters and stability of the spinel compounds in relation to the ionic radii and electronegativities of constituting chemical elements, Inorg. Chem. 53 (2014) 5088–5099. doi:10.1021/ic500200a.
[47] A. Khorsand Zak, W.H. Abd. Majid, M.E. Abrishami, R. Yousefi, X-ray analysis of ZnO nanoparticles by Williamson-Hall and size-strain plot methods, Solid State Sci. 13 (2011) 251–256. doi:10.1016/j.solidstatesciences.2010.11.024.
[48] R. Sivakami, S. Dhanuskodi, R. Karvembu, Estimation of lattice strain in nanocrystalline RuO 2 by Williamson – Hall and size – strain plot methods, Spectrochim. Acta Part A Mol. Biomol. Spectrosc. 152 (2016) 43–50. doi:10.1016/j.saa.2015.07.008.
[49] J.F. Nye, Physical Properties of Crystals: Their Representation by Tensors and Matrices, Oxford, New York, 1985.
[50] K.A. Avramenko, V.P. Bryksa, T.L. Petrenko, V.P. Kladko, H. V. Stanchu, A.E. Belyaev, C. Deparis, J. Zuñiga-Pérez, C. Morhain, Influence of strain relaxation on the relative orientation of ZnO and ZnMnO wurtzite lattice with respect to sapphire substrates, Mater. Res. Express. 3 (2016) 1–16. doi:10.1088/2053-1591/3/9/095902.
[51] I. Navas, S. Sreedhar, H. Kohler, R. Philip, R. Vinodkumar, V.P. Mahadevan Pillai, ZnO-Modified MoO3 Nano-Rods, -Wires, -Belts and -Tubes:

Photophysical and Nonlinear Optical Propertiess, J. Phys. Chem. C. 117 (2013) 7818–7829. doi:10.1021/jp311394y.

[52] I. Calizo, K.A. Alim, V.A. Fonoberov, S. Krishnakumar, M. Shamsa, Micro-Raman spectroscopic characterization of ZnO quantum dots , nanocrystals and nanowires, in: Proc. SPIE, 2007: p. 64810N. doi:10.1117/12.713648.

[53] M. Šćepanović, M. Grujić-Brojčin, K. Vojisavljević, S. Bernik, T. Srećković, Raman study of structural disorder in ZnO nanopowders, J. Raman Spectrosc. 41 (2009) 914–921. doi:10.1002/jrs.2546.

[54] R. Cuscó, E. Alarcón-Lladó, J. Ibáñez, L. Artús, J. Jiménez, B. Wang, M.J. Callahan, Temperature dependence of Raman scattering in ZnO, Phys. Rev. B. 75 (2007) 165202. doi:10.1103/PhysRevB.75.165202.

[55] Y. Il Kim, K. Page, A.M. Limarga, D.R. Clarke, R. Seshadri, Evolution of local structures in polycrystalline Zn1-x Mgx O ($0 \leq x \leq 0.15$) studied by Raman spectroscopy and synchrotron x-ray pair-distribution-function analysis, Phys. Rev. B - Condens. Matter Mater. Phys. 76 (2007) 1–10. doi:10.1103/PhysRevB.76.115204.

[56] V. Lughi, D.R. Clarke, Transformation of electron-beam physical vapor-deposited 8 wt% yttria-stabilized zirconia thermal barrier coatings, J. Am. Ceram. Soc. 88 (2005) 2552–2558. doi:10.1111/j.1551-2916.2005.00452.x.

[57] O.A. Yassin, S.N. Alamri, A.A. Joraid, Effect of particle size and laser power on the Raman spectra of CuAlO2delafossite nanoparticles, J. Phys. D. Appl. Phys. 46 (2013). doi:10.1088/0022-3727/46/23/235301.

[58] K. Samanta, P. Bhattacharya, R.S. Katiyar, W. Iwamoto, P.G. Pagliuso, C. Rettori, Raman scattering studies in dilute magnetic semiconductor Zn1-x Cox O, Phys. Rev. B - Condens. Matter Mater. Phys. 73 (2006) 1–5. doi:10.1103/PhysRevB.73.245213.

[59] J. Serrano, F.J. Manjón, A.H. Romero, F. Widulle, R. Lauck, M. Cardona, Dispersive Phonon Linewidths: The E2 Phonons of ZnO, Phys. Rev. Lett. 90 (2003) 4. doi:10.1103/PhysRevLett.90.055510.

[60] M.S. Tomar, R. Melgarejo, Synthesis of Zn 1 − x Mg x O and its structural characterization, J. Mater. Res. 16 (2001) 903–906.

[61] T.H. Flemban, M.C. Sequeira, Z. Zhang, S. Venkatesh, E. Alves, K. Lorenz, I.S. Roqan, Identifying the influence of the intrinsic defects in Gd-doped ZnO thin-films, J. Appl. Phys. 119 (2016). doi:10.1063/1.4941434.

[62] T.J. Castro, S.W. Da Silva, F. Nakagomi, N.S. Moura, J. Franco, P.C. Morais, Structural and magnetic properties of ZnO-CoFe<inf>2</inf>O<inf>4</inf> nanocomposites, J. Magn. Magn. Mater. 389 (2015) 27–33. doi:10.1016/j.jmmm.2015.04.036.

[63] S. Sahoo, G.L. Sharma, R.S. Katiyar, Raman spectroscopy to probe residual stress in ZnO nanowire, J. Raman Spectrosc. 43 (2012) 72–75. doi:10.1002/jrs.3004.

[64] R. Sánchez Zeferino, M. Barboza Flores, U. Pal, Photoluminescence and raman scattering in ag-doped zno nanoparticles, J. Appl. Phys. 109 (2011) 1–7. doi:10.1063/1.3530631.

[65] W. Shan, W. Walukiewicz, J.W. Ager, K.M. Yu, H.B. Yuan, H.P. Xin, G. Cantwell, J.J. Song, Nature of room-temperature photoluminescence in ZnO, Appl. Phys. Lett. 191911 (2005) 86–89. doi:10.1063/1.1923757.

[66] H. Rotella, Y. Mazel, S. Brochen, A. Valla, A. Pautrat, C. Licitra, N. Rochat, C. Sabbione, G. Rodriguez, E. Nolot, J. Phys. D: Appl. Phys. 50 (2017) 485106.

[67] Q. Fan, J. Yang, Y. Yu, J. Zhang, J. Cao, Chemical Engineering Transactions 46

(2015) 985-990.
[68] M. Willander, O. Nur, J.R. Sadaf, M.I. Qadir, S. Zaman, A. Zainelabdin, N. Bano, I. Hussain, Luminescence from Zinc Oxide Nanostructures and Polymers and their Hybrid Devices, Materials (Basel). 3 (2010) 2643–2667. doi:10.3390/ma3042643.
[69] F. Oba, M. Choi, I. Tanaka, Point defects in ZnO: an approach from first principles, Sci. Technol. Adv. Mater. 12 (2011) 034302. doi:10.1088/1468-6996/12/3/034302.
[70] F. Kayaci, S. Vempati, I. Donmez, N. Biyikli, T. Uyar, Role of zinc interstitials and oxygen vacancies of ZnO in photocatalysis: A bottom-up approach to control the defect density, Nanoscale. 6 (2014) 10224–10234. doi:10.1039/C4NR01887G.
[71] M.D. McCluskey, S.J. Jokela, Defects in ZnO, J. Appl. Phys. 106 (2009). doi:10.1063/1.3216464.

Figure Captions

Figure No. 1**.** Fig. 1 SEM micrographs of synthesized powders. (a) ZnO; (b,c) ZnO:Al; (d,e) ZnO:Sr and (f,g) a close view of ZnO:Al 1% and ZnO:Sr 4% respectively.

Figure No. 2**.** Fig 2. EDX spectra from synthesized powders. (a) ZnO; (b) ZnO:Al 1%; (c) ZnO:Al 4%; (d) ZnO:Sr 1% and (e) ZnO:Sr 4%.

Figure No. 3**.** Fig. 3. XRD patterns from ZnO (bottom) and from ZnO:M (M=Al and Sr) with 1 and 4 % of M nominal content.

Figure No. 4. The Williamson-Hall plot using the Uniform Stress Deformation Model (USDM) for ZnO, ZnO:Al and ZnO:Sr. The red line corresponding to the linear fit; the crystallite size D is estimated from the line intersection with the axis and the strain σ is estimated from the slope.

Figure No. 5. Fig. 5. Micro-Raman spectra for ZnO, ZnO:Al and ZnO:Sr.

Figure No. 6. (a-e). The E_2^{low} mode of studied samples and its corresponding fit with Breit-Wigner function. (f) ω_0 of E_2^{low} mode extracted from the fits as function of the Al and Sr nominal contents.

Figure No. 7. (a-e). The E_2^{high} mode of studied samples and its corresponding fit with Breit-Wigner function. (f) ω_0 of E_2^{high} mode extracted from the fits as function of the Al and Sr nominal contents.

Figure No. 8 (a-b). Photoluminescence spectra of the ZnO, ZnO:Al and ZnO:Sr samples. (c) Normalized UV emission. (d) Normalized visible emission for all the samples.

Figure No. 9. Gaussian fit of UV emission from ZnO, ZnO:Al and ZnO:Sr samples. For ZnO:Al samples, it was necessary to fit with three Gaussian components, while for ZnO and ZnO:Sr, the best fits were achieved with two Gaussian components.

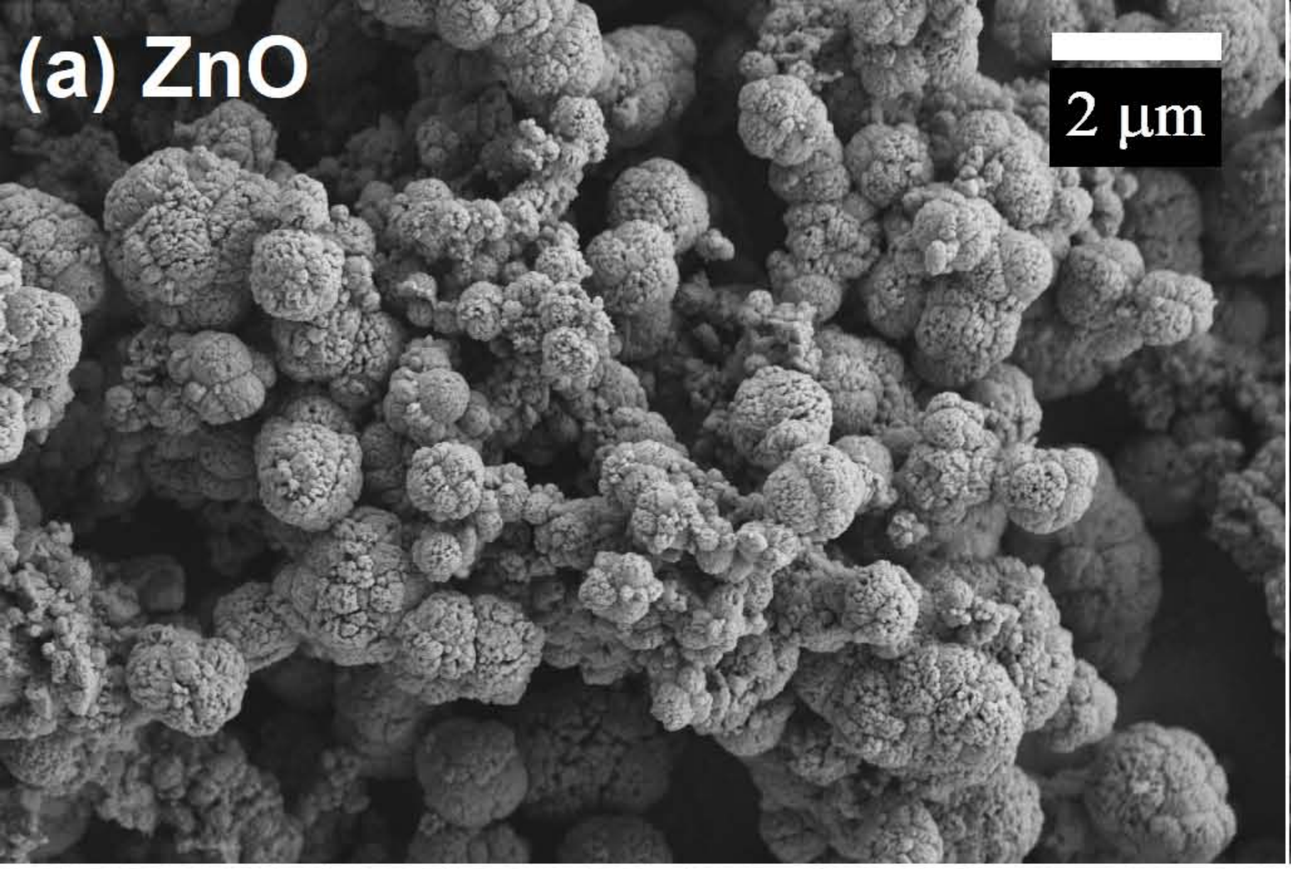
(a) ZnO
2 µm

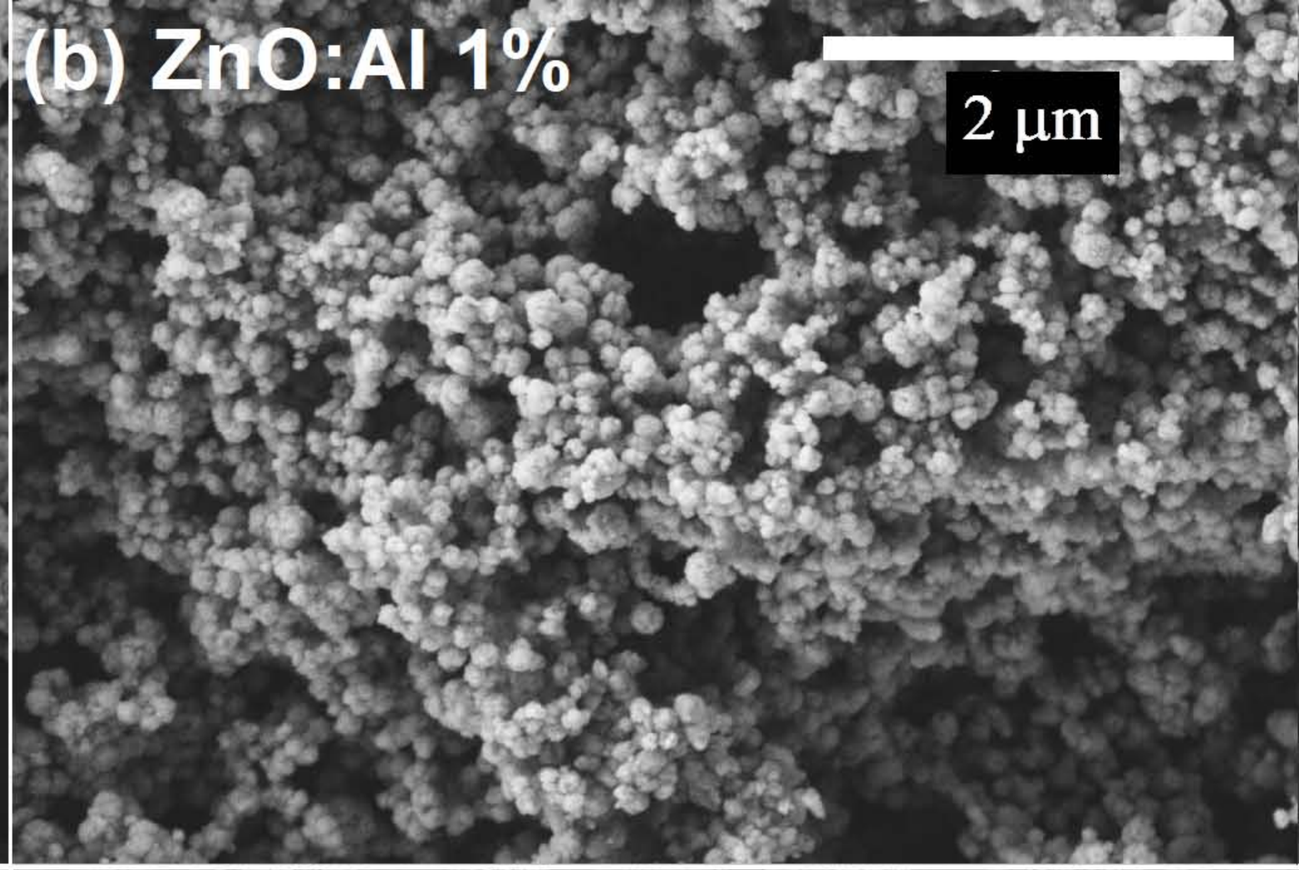
(b) ZnO:Al 1%
2 µm

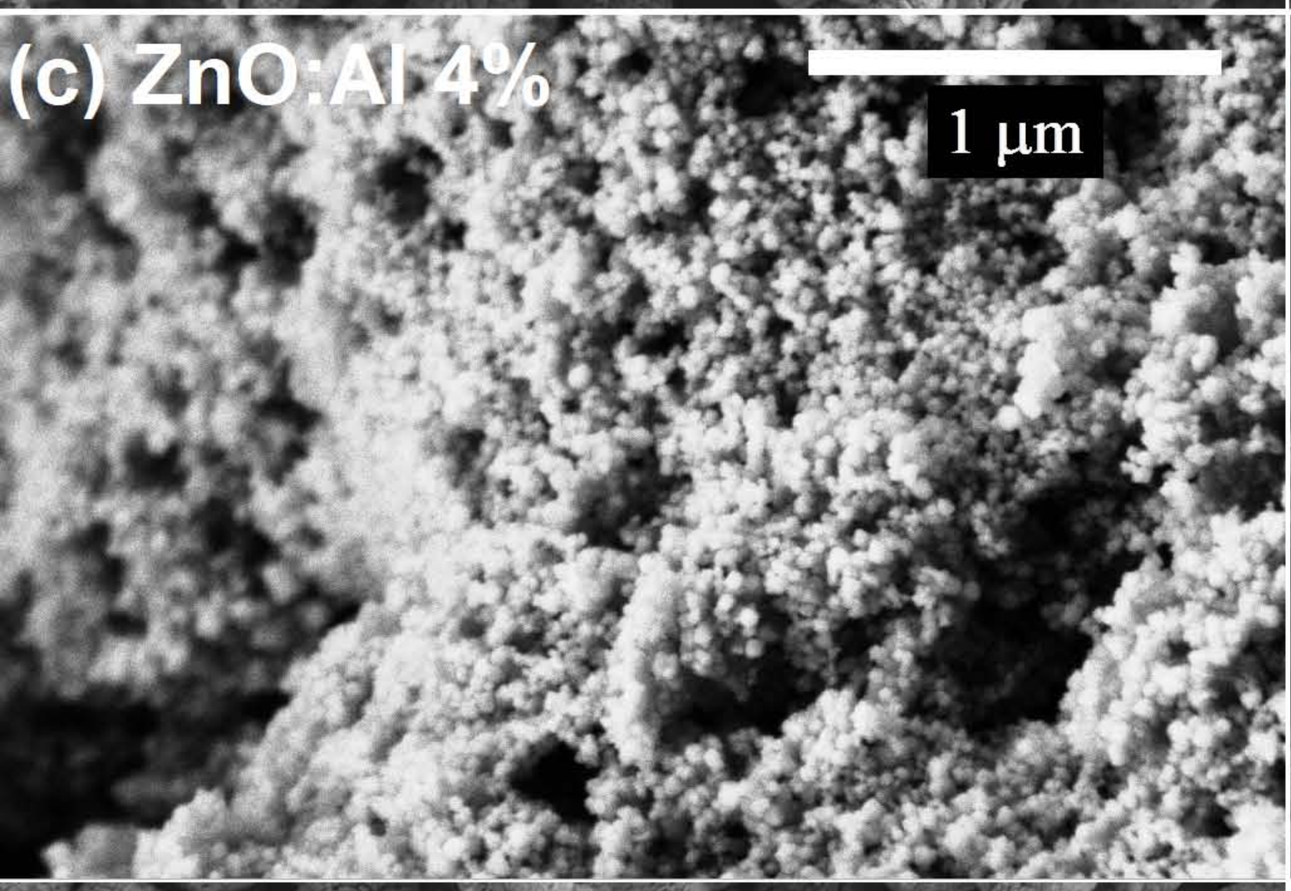
(c) ZnO:Al 4%
1 µm

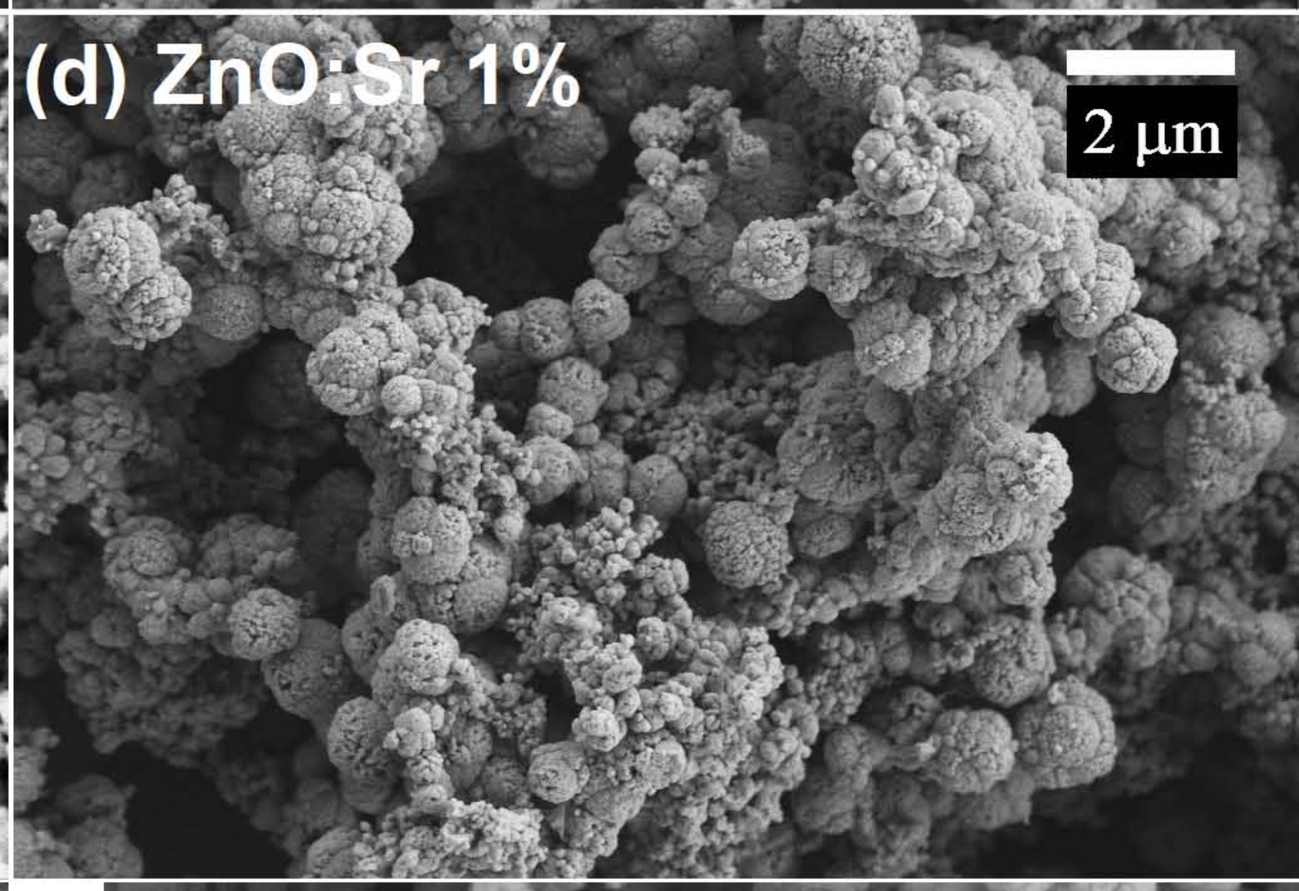
(d) ZnO:Sr 1%
2 µm

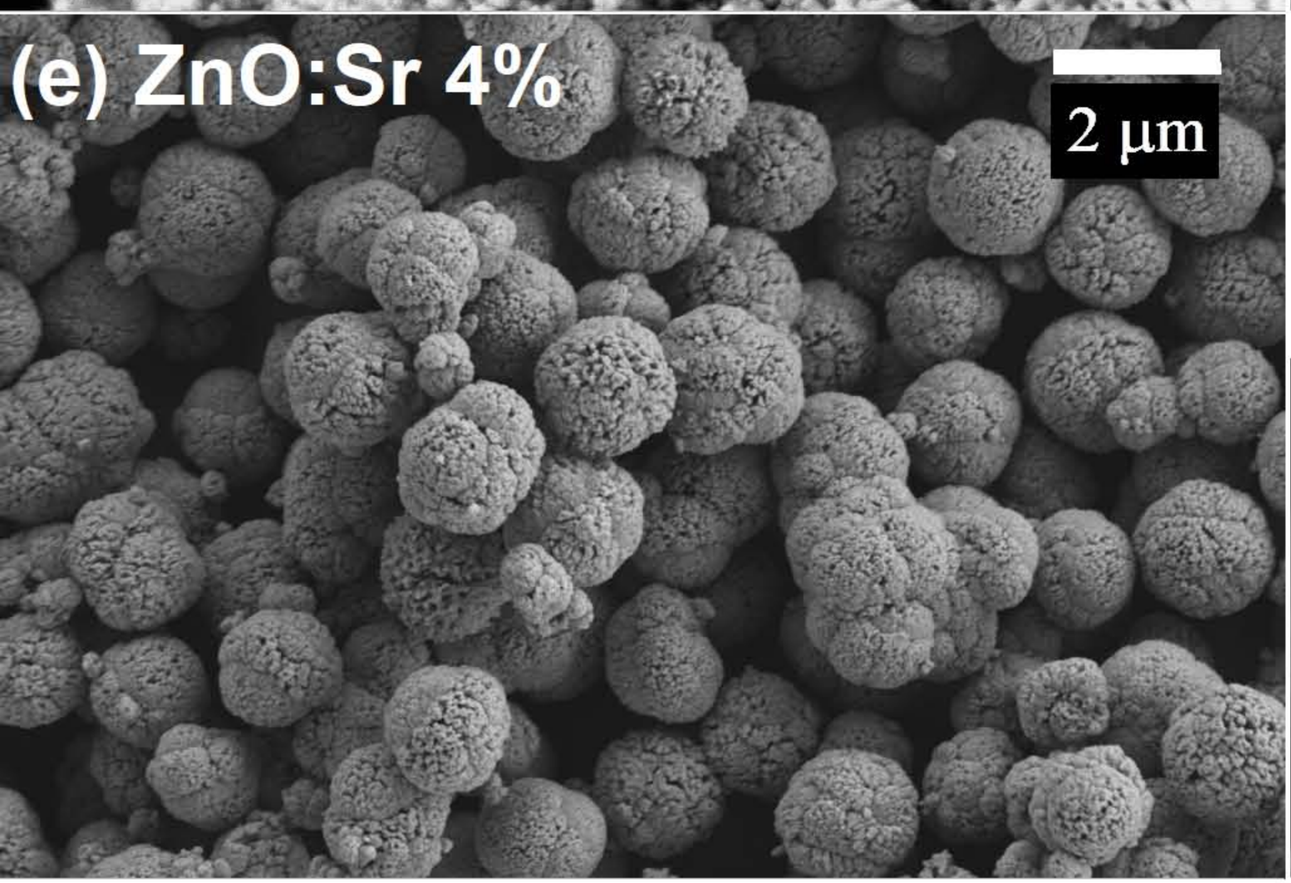
(e) ZnO:Sr 4%
2 µm

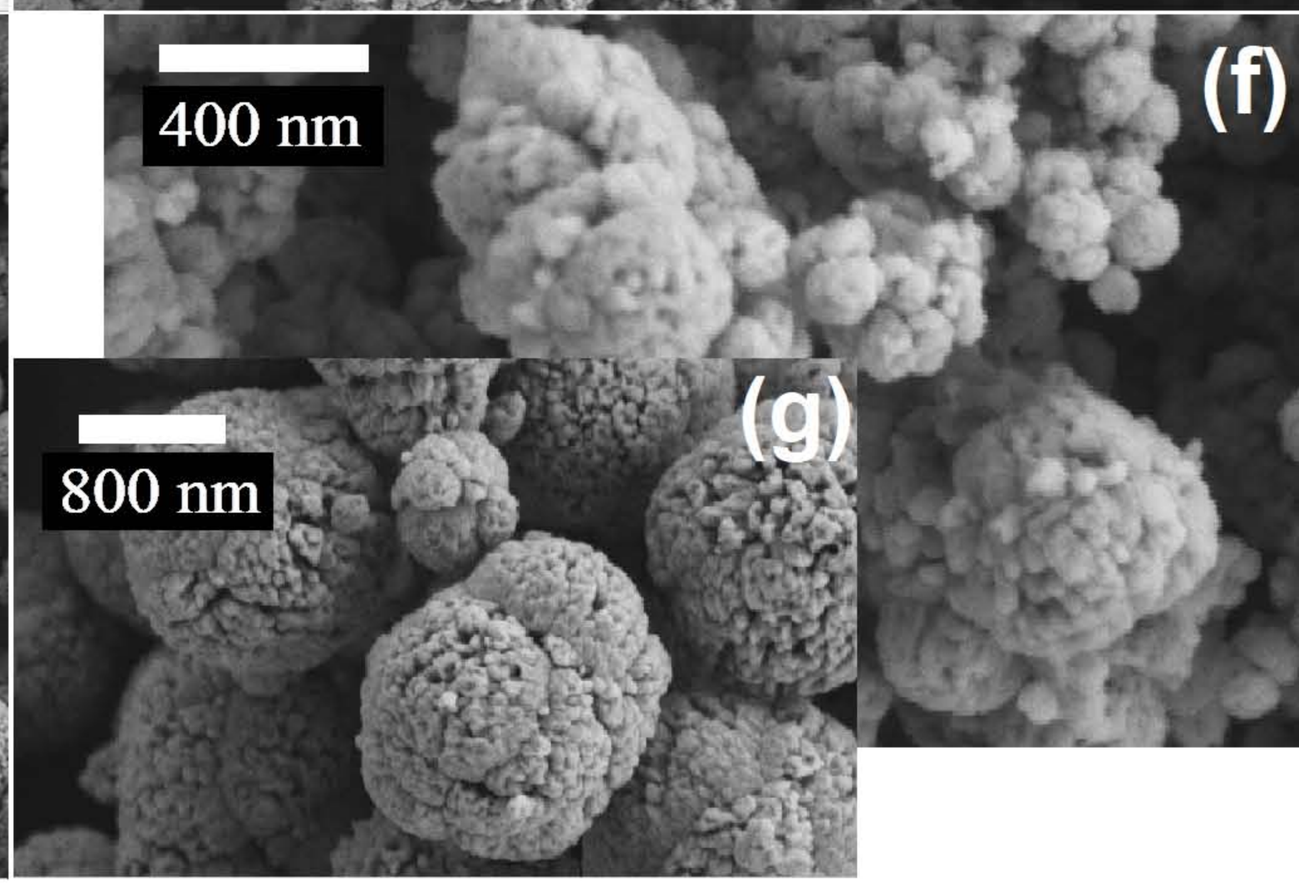
400 nm
(f)
800 nm
(g)

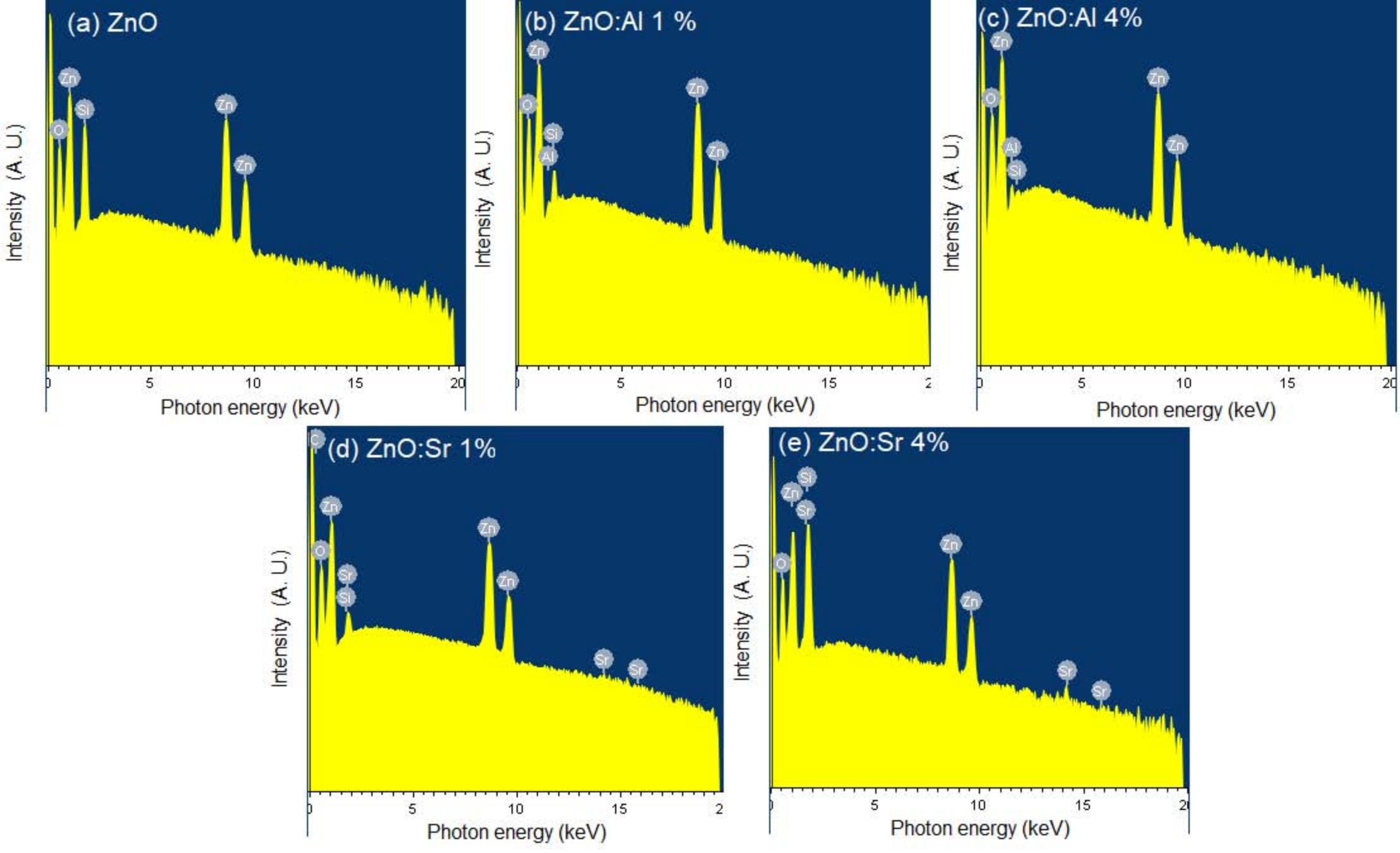
(a) ZnO
(b) ZnO:Al 1 %
(c) ZnO:Al 4%
(d) ZnO:Sr 1%
(e) ZnO:Sr 4%
Intensity (A. U.)
Photon energy (keV)
Zn
O
Si
Al
Sr
0
5
10
15
20

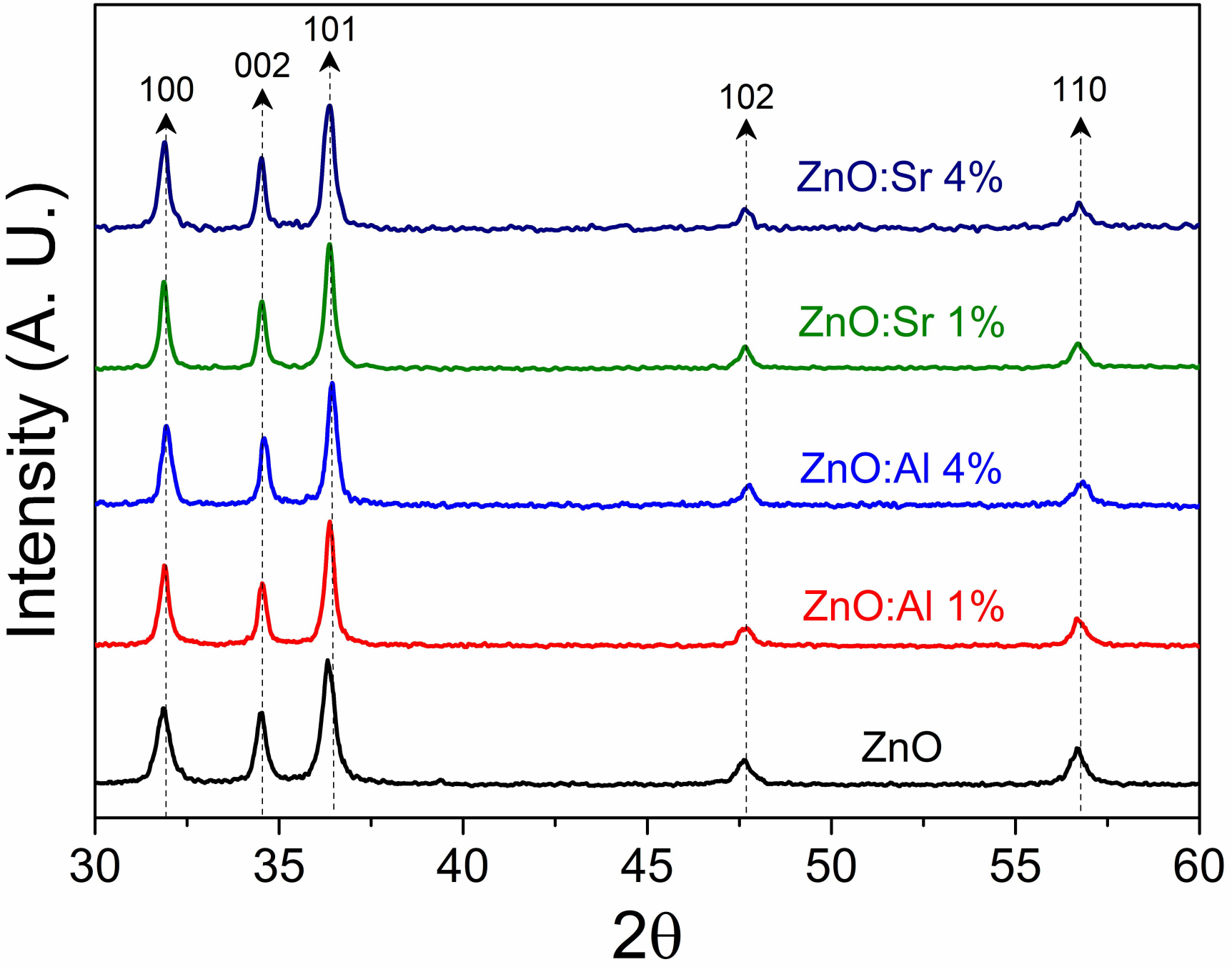
100
002
101
102
110
ZnO:Sr 4%
ZnO:Sr 1%
ZnO:Al 4%
ZnO:Al 1%
ZnO
Intensity (A. U.)
30
35
40
45
50
55
60
2θ

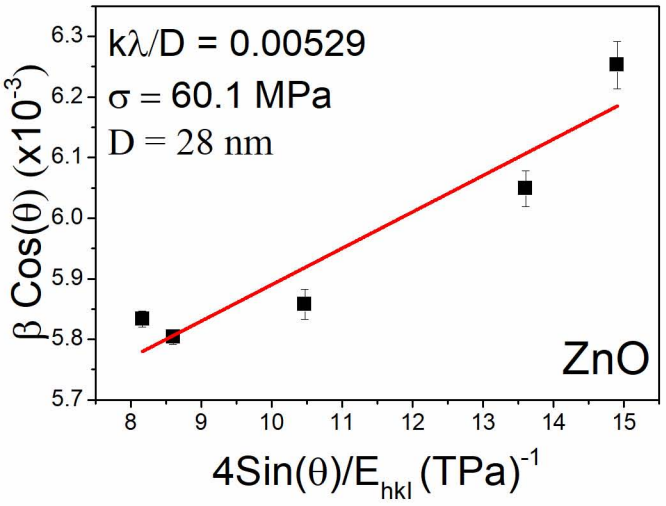
kλ/D = 0.00529
σ = 60.1 MPa
D = 28 nm
ZnO
β Cos(θ) (x10-3)
4Sin(θ)/Ehkl (TPa)-1

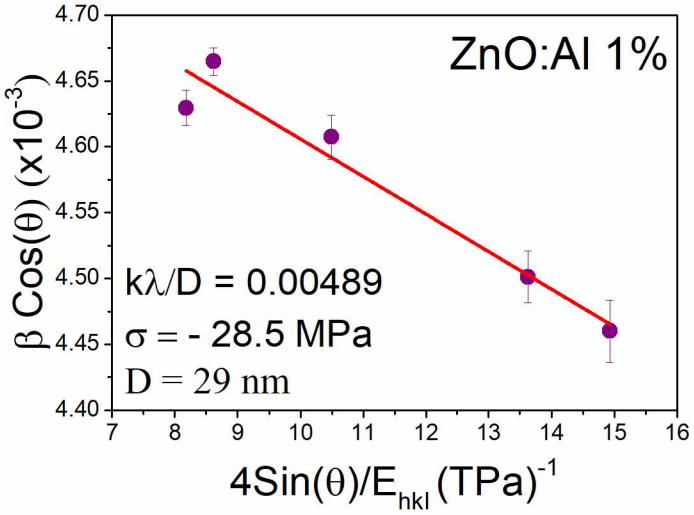
ZnO:Al 1%
kλ/D = 0.00489
σ = - 28.5 MPa
D = 29 nm
β Cos(θ) (x10-3)
4Sin(θ)/Ehkl (TPa)-1

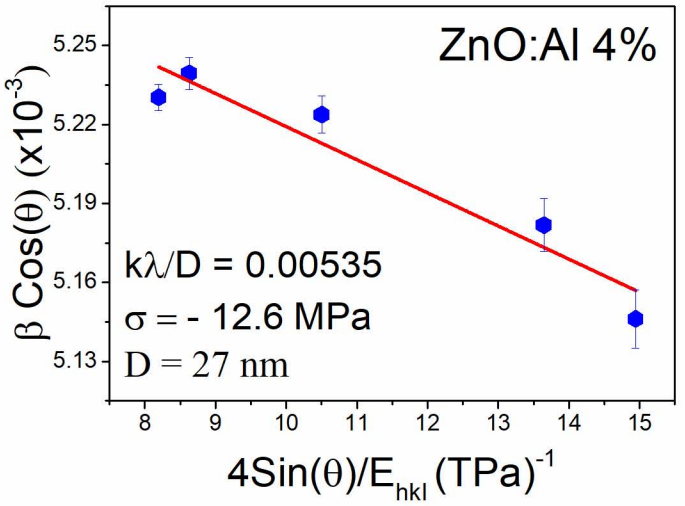
ZnO:Al 4%
kλ/D = 0.00535
σ = - 12.6 MPa
D = 27 nm
β Cos(θ) (x10-3)
4Sin(θ)/Ehkl (TPa)-1

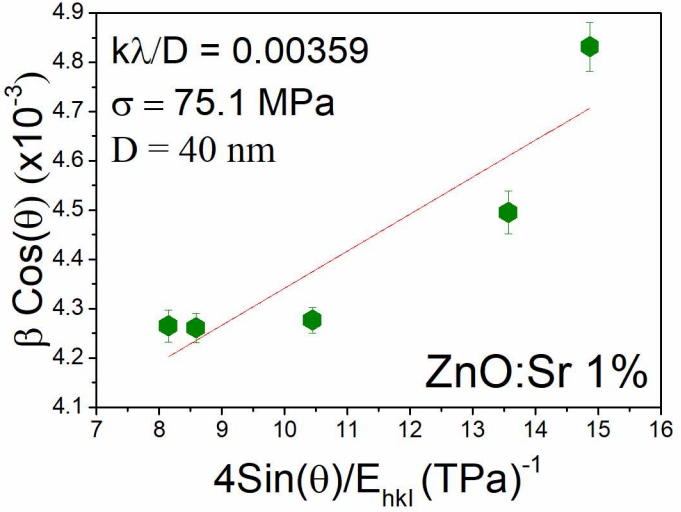
kλ/D = 0.00359
σ = 75.1 MPa
D = 40 nm
ZnO:Sr 1%
β Cos(θ) (x10-3)
4Sin(θ)/Ehkl (TPa)-1

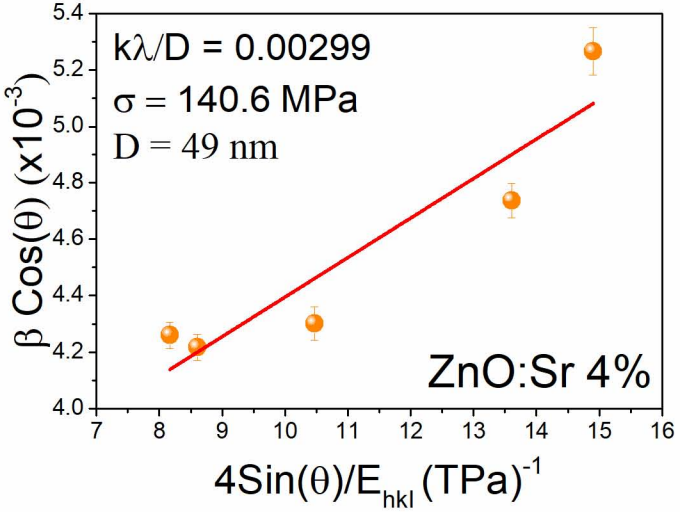
kλ/D = 0.00299
σ = 140.6 MPa
D = 49 nm
ZnO:Sr 4%
β Cos(θ) (x10-3)
4Sin(θ)/Ehkl (TPa)-1

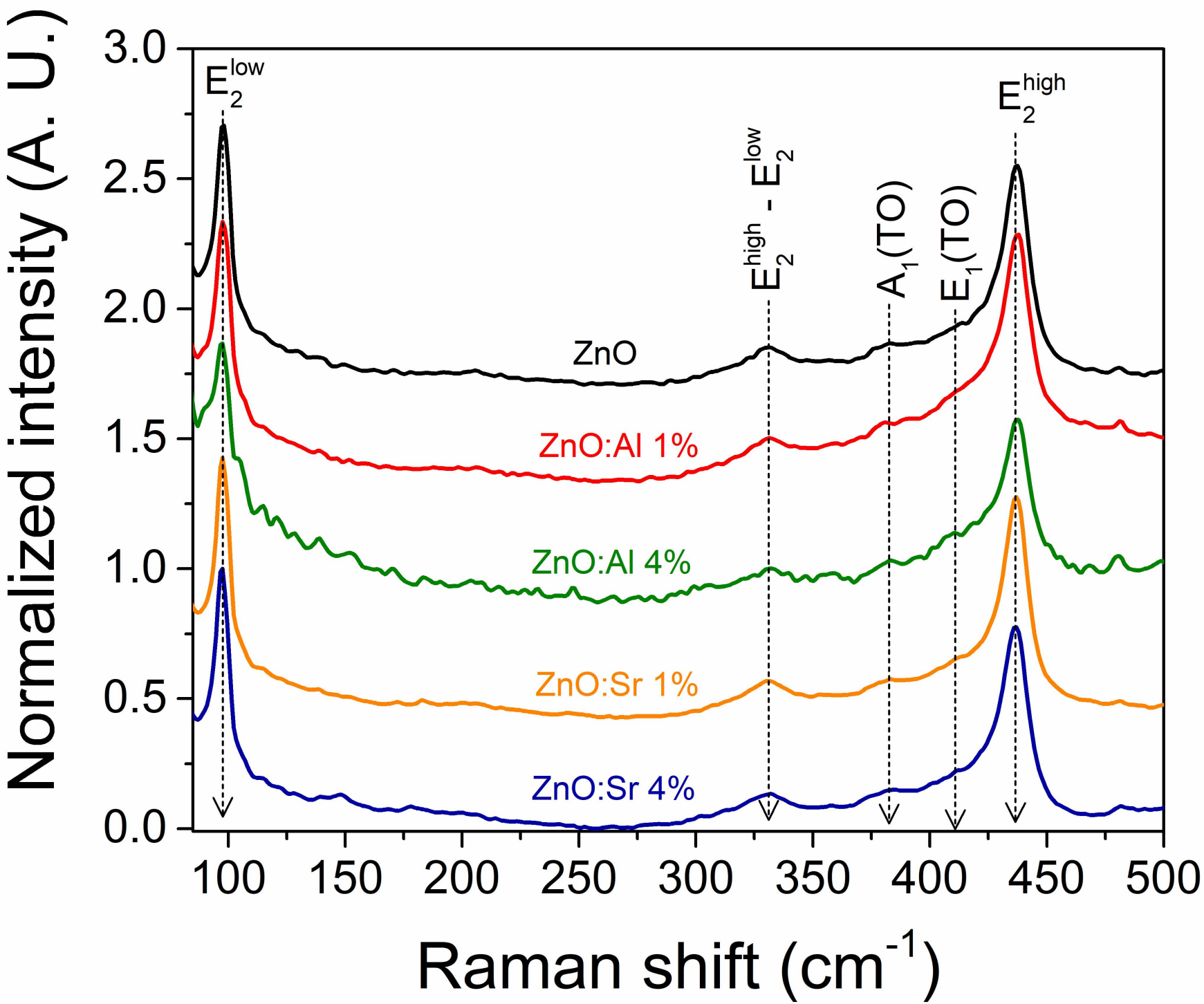
Normalized intensity (A. U.)
Raman shift (cm-1)
3.0
2.5
2.0
1.5
1.0
0.5
0.0
100
150
200
250
300
350
400
450
500
E2low
E2high - E2low
A1(TO)
E1(TO)
E2high
ZnO
ZnO:Al 1%
ZnO:Al 4%
ZnO:Sr 1%
ZnO:Sr 4%

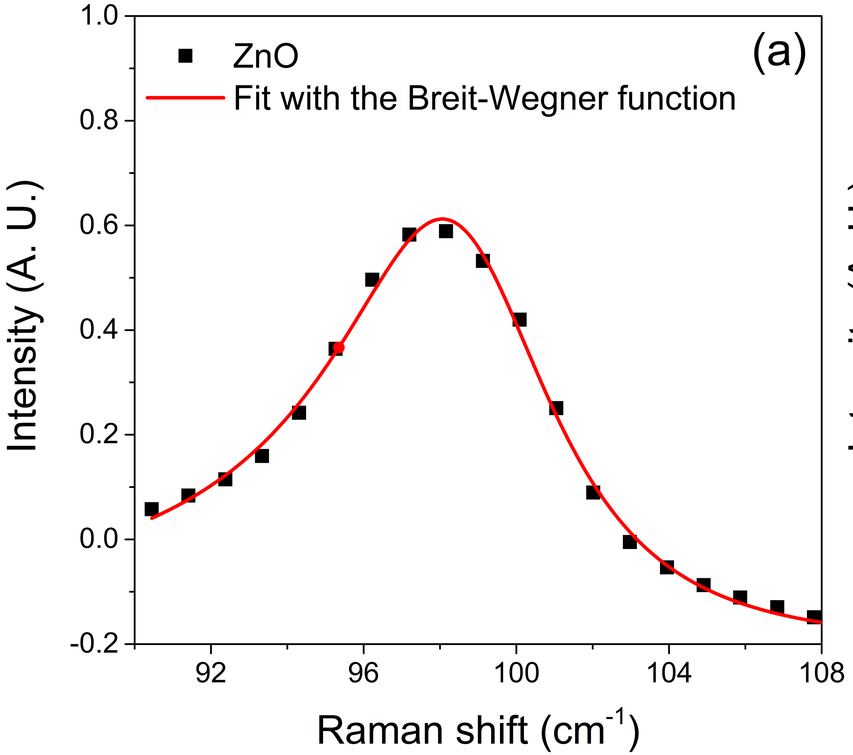
ZnO
Fit with the Breit-Wegner function
(a)
Intensity (A. U.)
Raman shift (cm-1)

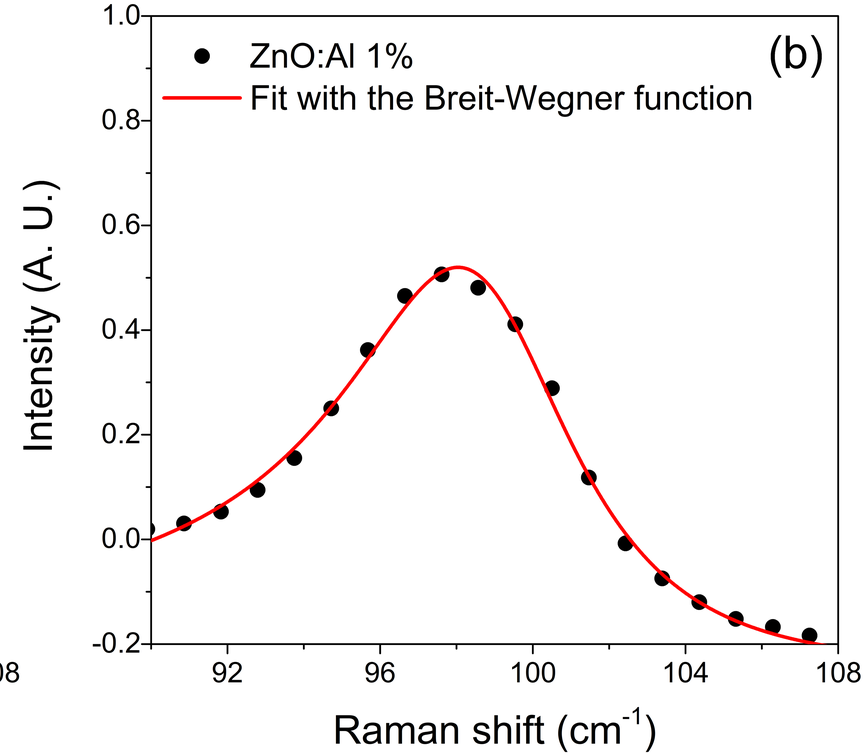
ZnO:Al 1%
Fit with the Breit-Wegner function
(b)
Intensity (A. U.)
Raman shift (cm-1)

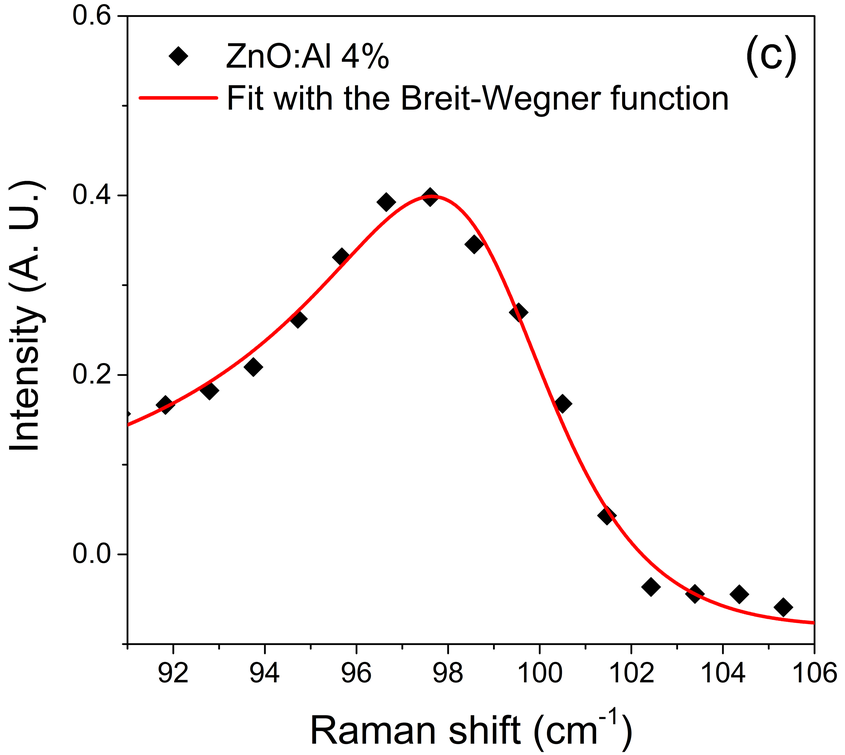
ZnO:Al 4%
Fit with the Breit-Wegner function
(c)
Intensity (A. U.)
Raman shift (cm-1)

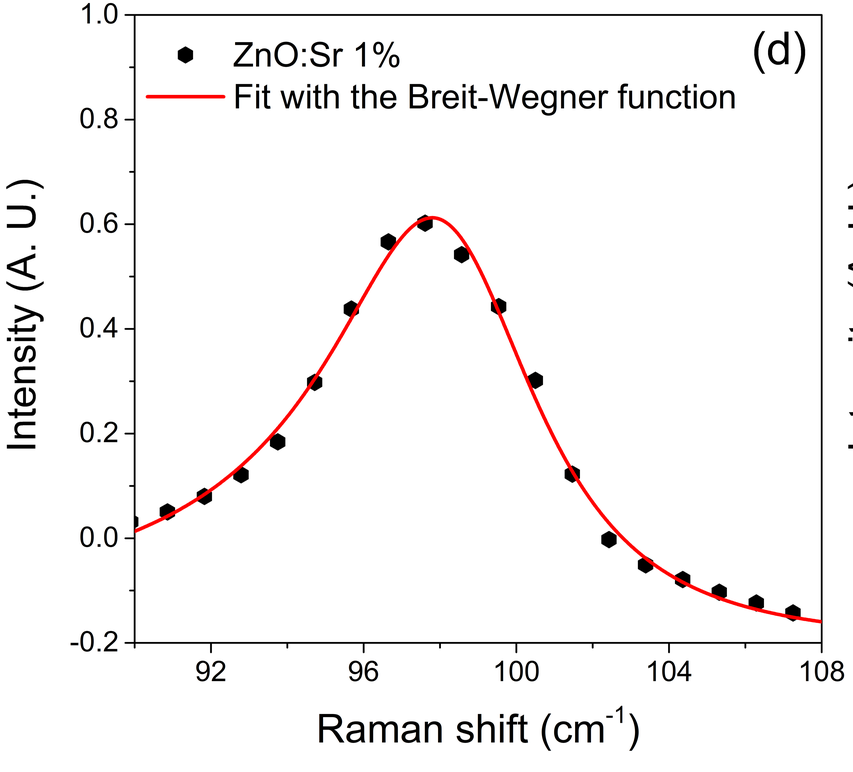
ZnO:Sr 1%
Fit with the Breit-Wegner function
(d)
Intensity (A. U.)
Raman shift (cm-1)

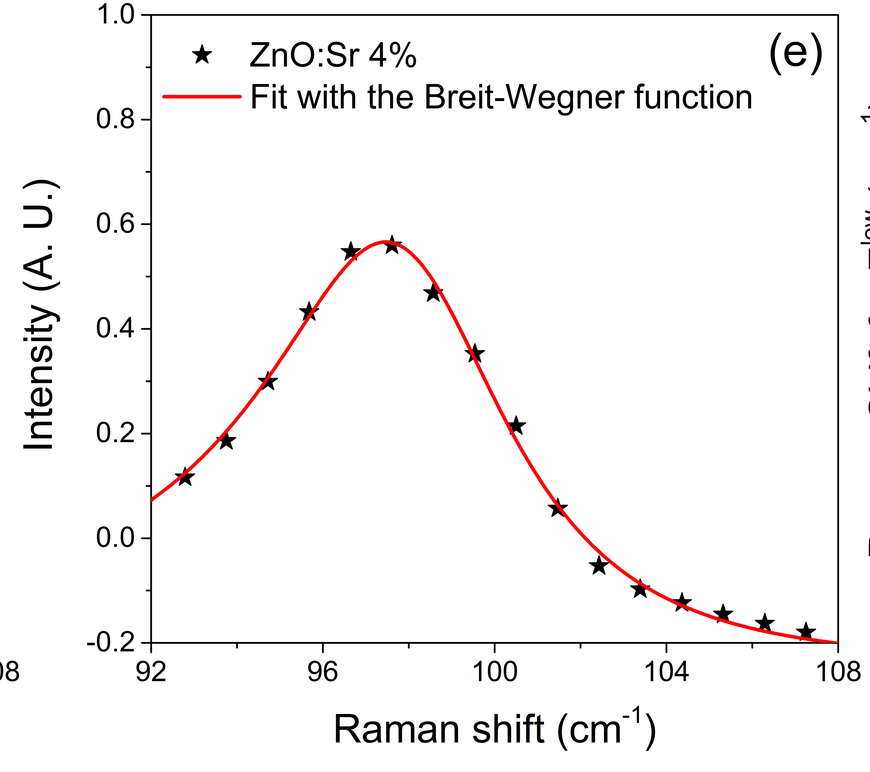
ZnO:Sr 4%
Fit with the Breit-Wegner function
(e)
Intensity (A. U.)
Raman shift (cm-1)

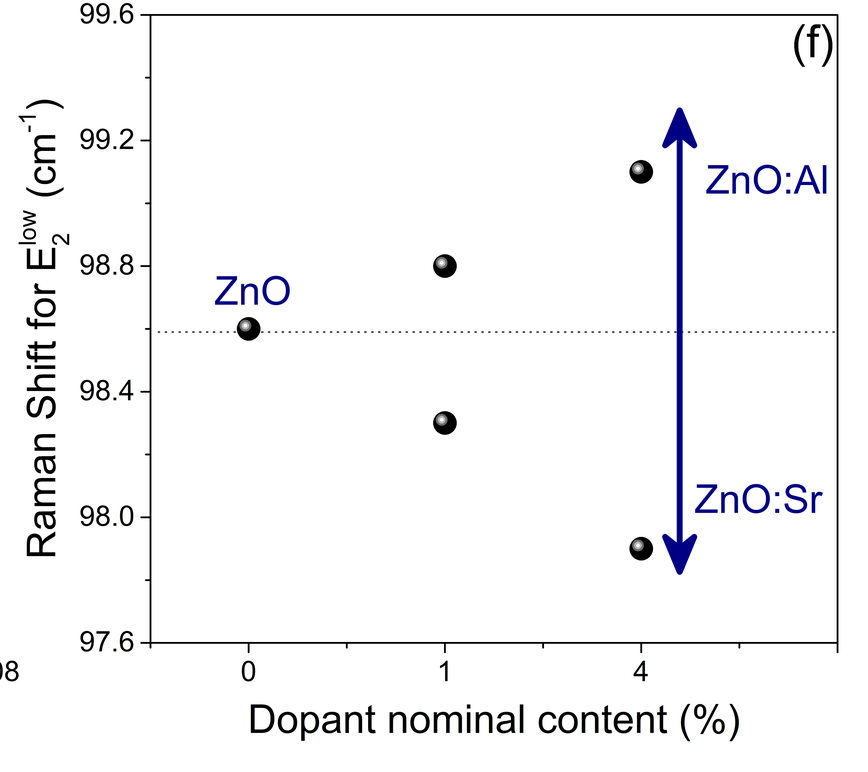
(f)
ZnO
ZnO:Al
ZnO:Sr
Raman Shift for E2low (cm-1)
Dopant nominal content (%)

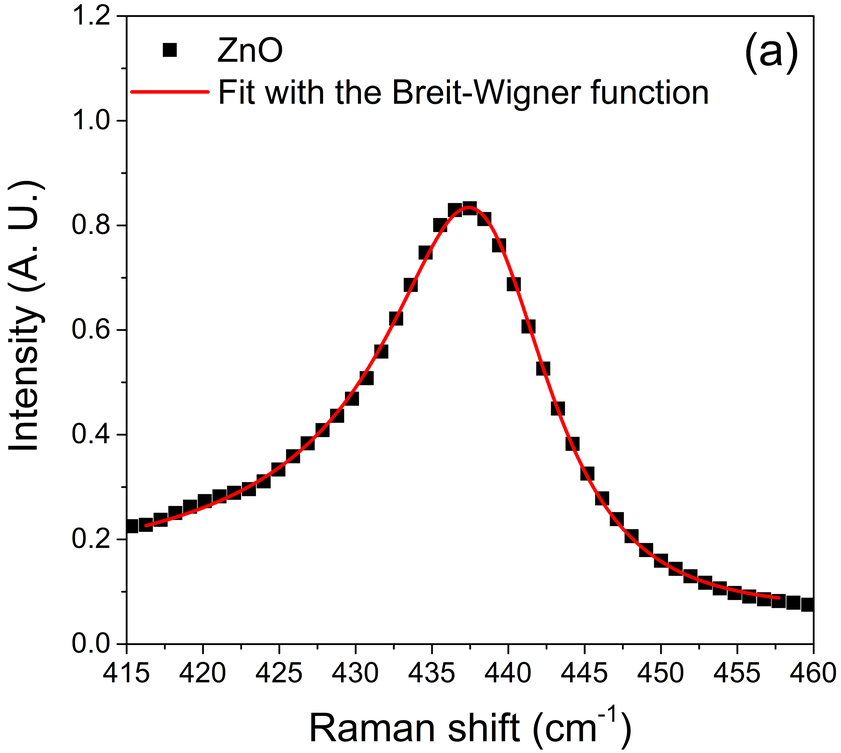
(a)
ZnO
Fit with the Breit-Wigner function
Intensity (A. U.)
Raman shift (cm-1)

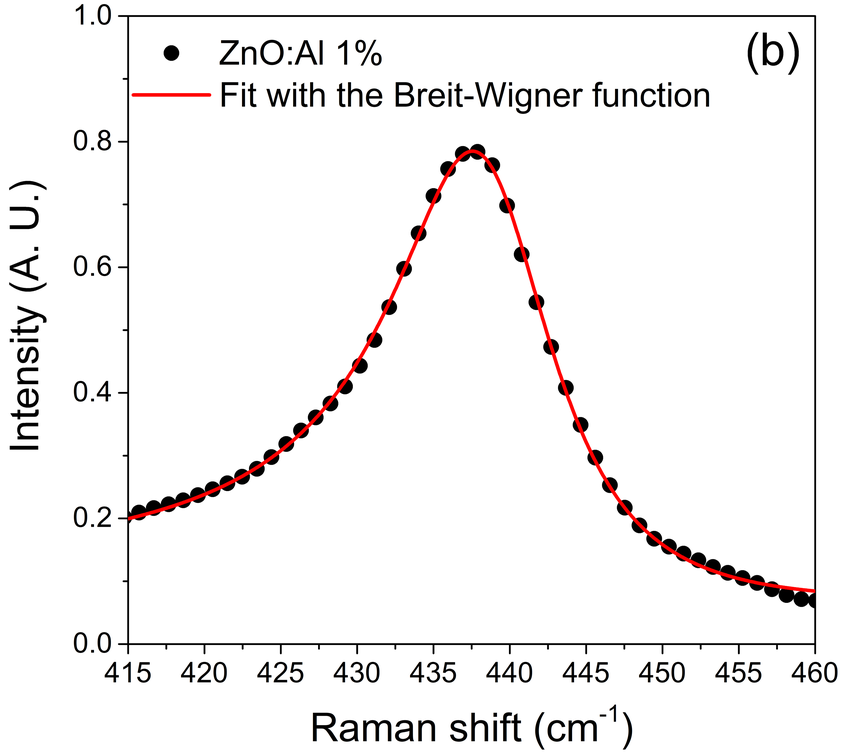
(b)
ZnO:Al 1%
Fit with the Breit-Wigner function
Intensity (A. U.)
Raman shift (cm-1)

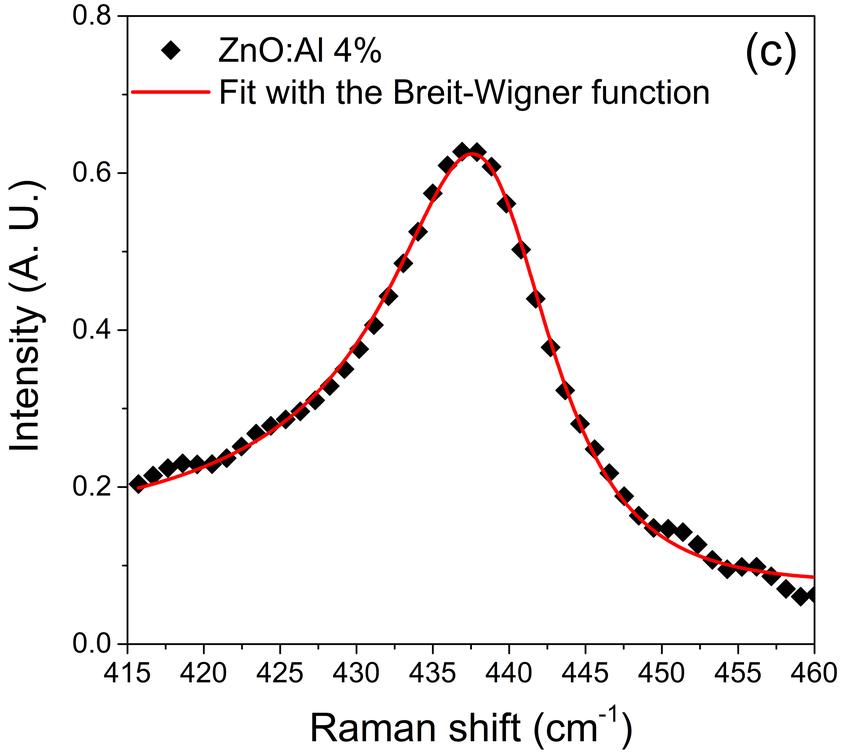
(c)
ZnO:Al 4%
Fit with the Breit-Wigner function
Intensity (A. U.)
Raman shift (cm-1)

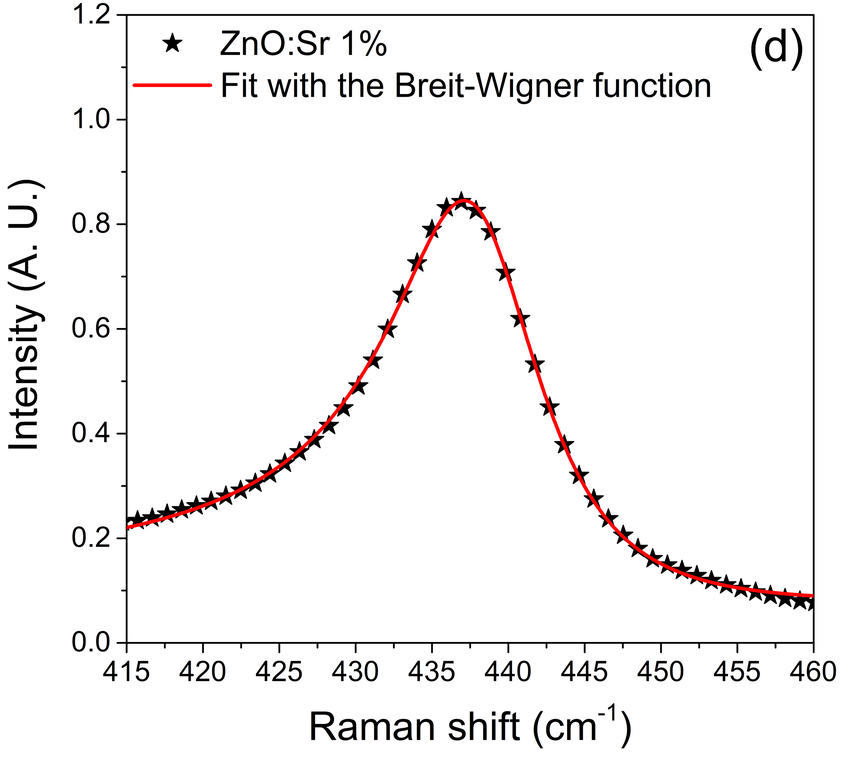
(d)
ZnO:Sr 1%
Fit with the Breit-Wigner function
Intensity (A. U.)
Raman shift (cm-1)

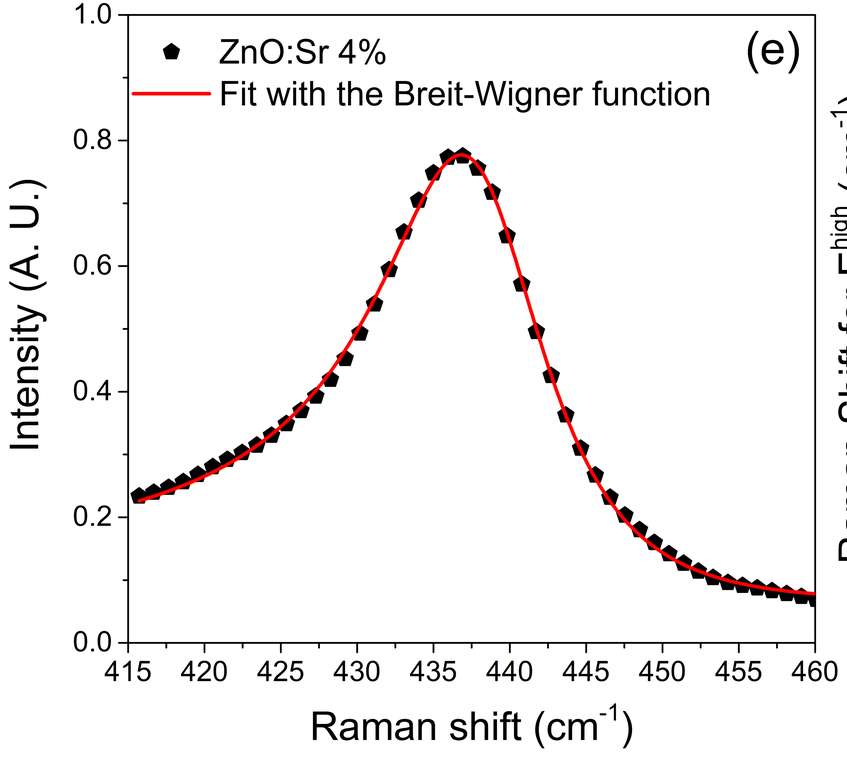
(e)
ZnO:Sr 4%
Fit with the Breit-Wigner function
Intensity (A. U.)
Raman shift (cm-1)

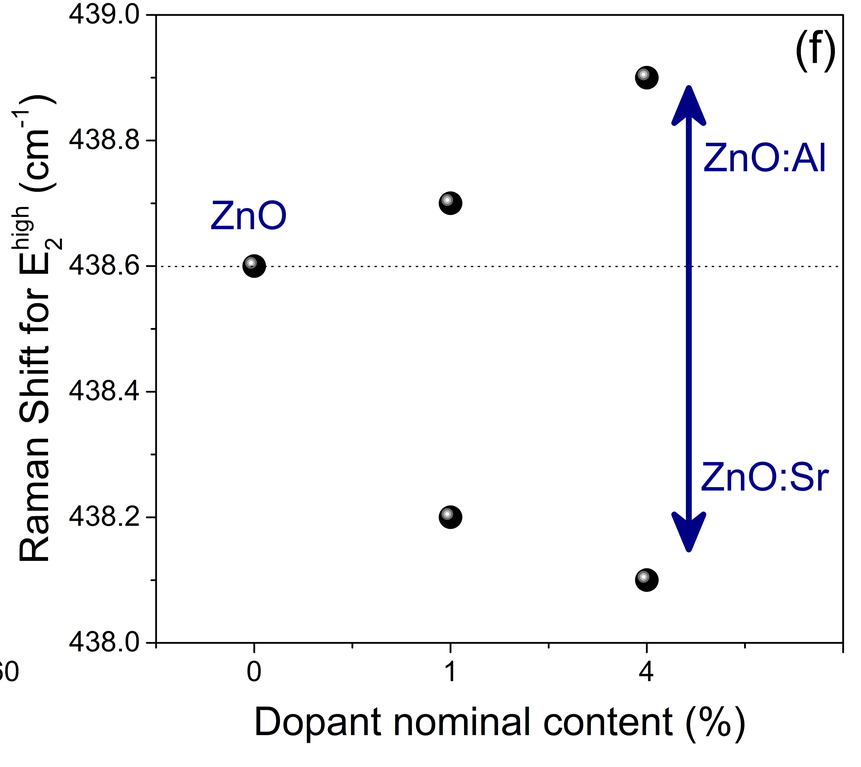
(f)
ZnO
ZnO:Al
ZnO:Sr
Raman Shift for E2high (cm-1)
Dopant nominal content (%)

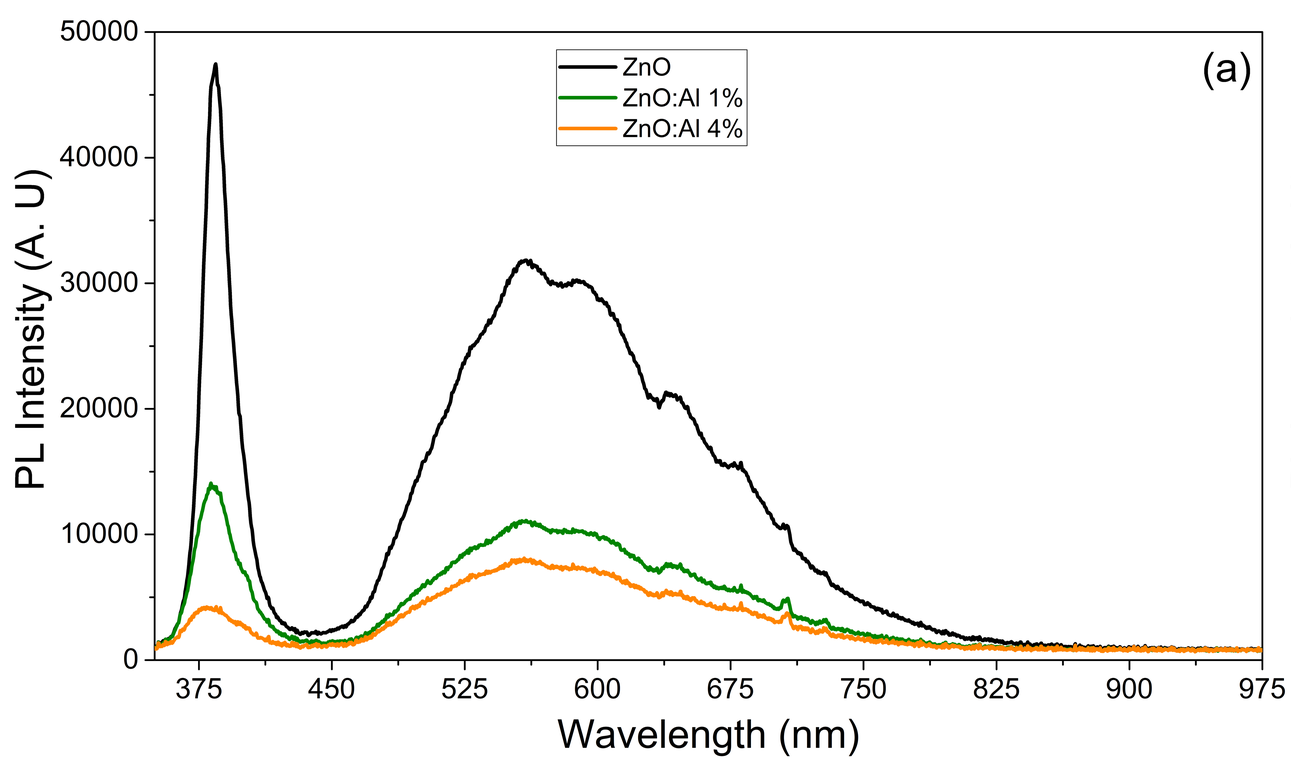
(a)
ZnO
ZnO:Al 1%
ZnO:Al 4%
PL Intensity (A. U)
Wavelength (nm)
0
10000
20000
30000
40000
50000
375
450
525
600
675
750
825
900
975

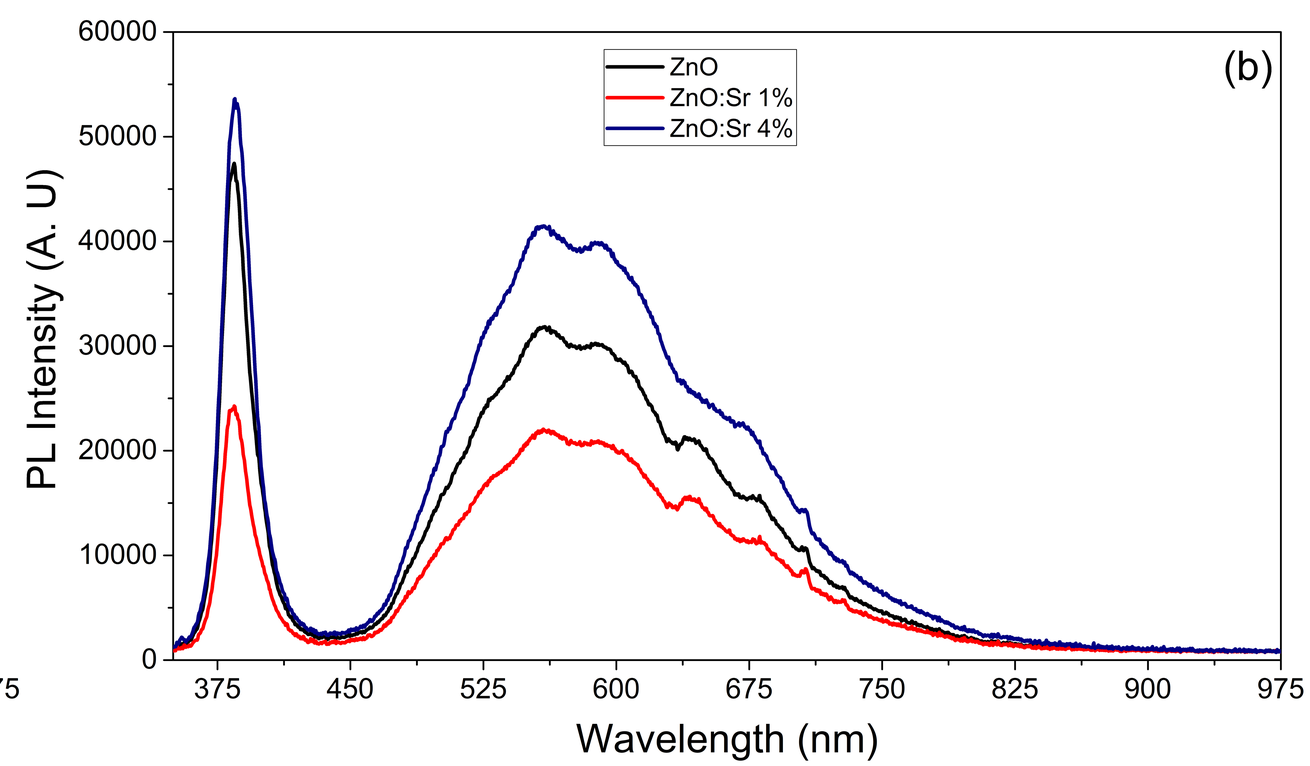
(b)
ZnO
ZnO:Sr 1%
ZnO:Sr 4%
PL Intensity (A. U)
Wavelength (nm)
0
10000
20000
30000
40000
50000
60000
375
450
525
600
675
750
825
900
975

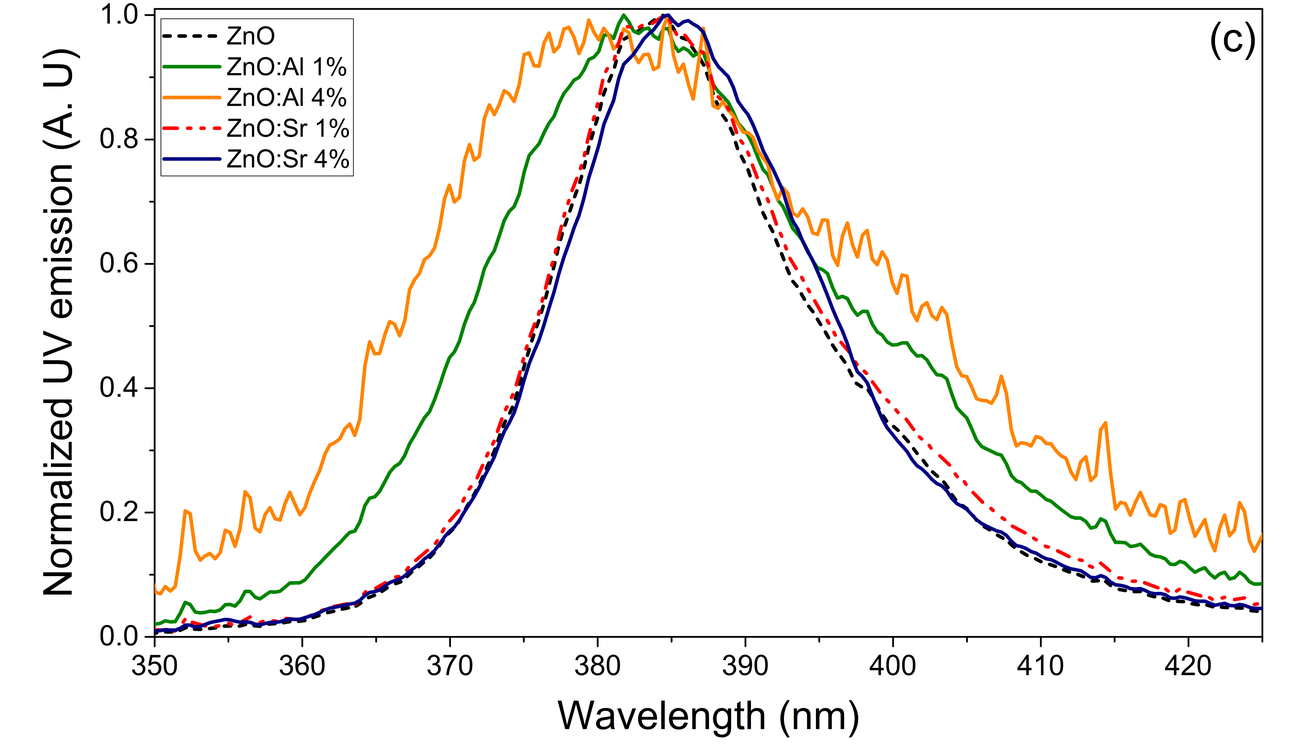
(c)
ZnO
ZnO:Al 1%
ZnO:Al 4%
ZnO:Sr 1%
ZnO:Sr 4%
Normalized UV emission (A. U)
Wavelength (nm)
0.0
0.2
0.4
0.6
0.8
1.0
350
360
370
380
390
400
410
420

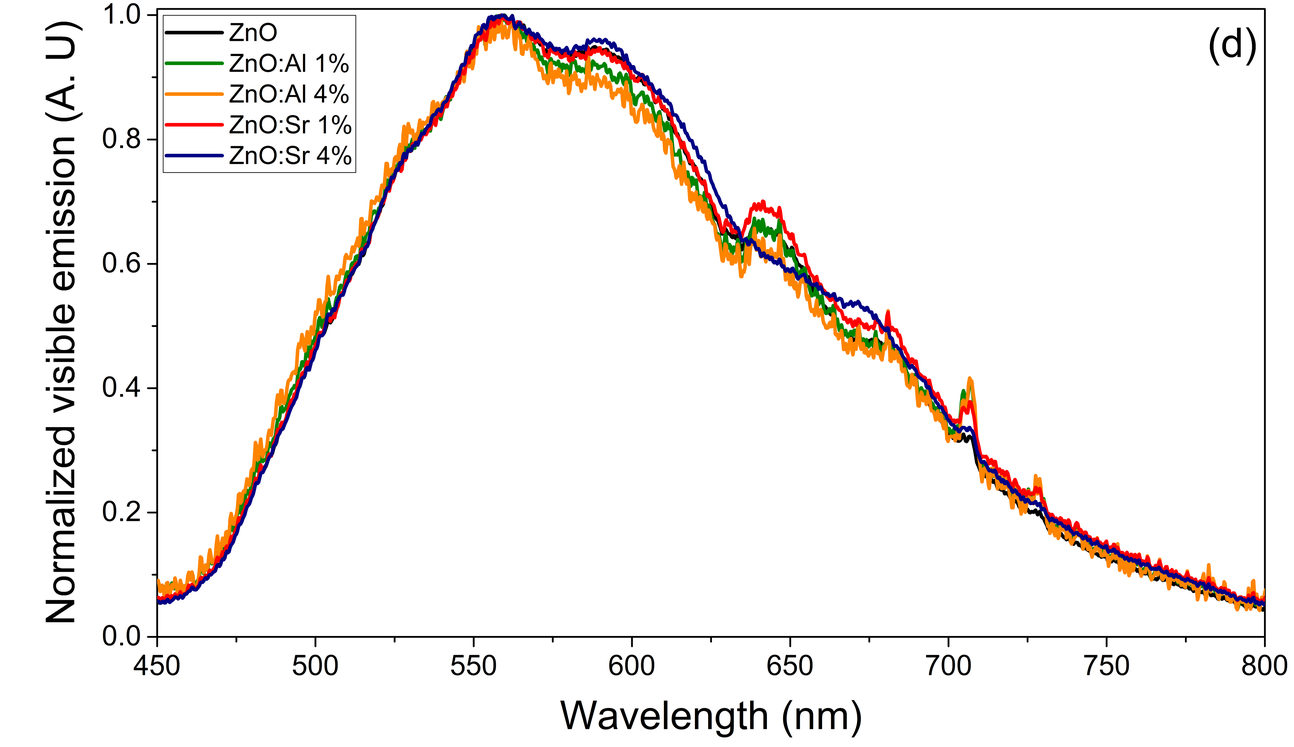
(d)
ZnO
ZnO:Al 1%
ZnO:Al 4%
ZnO:Sr 1%
ZnO:Sr 4%
Normalized visible emission (A. U)
Wavelength (nm)
0.0
0.2
0.4
0.6
0.8
1.0
450
500
550
600
650
700
750
800

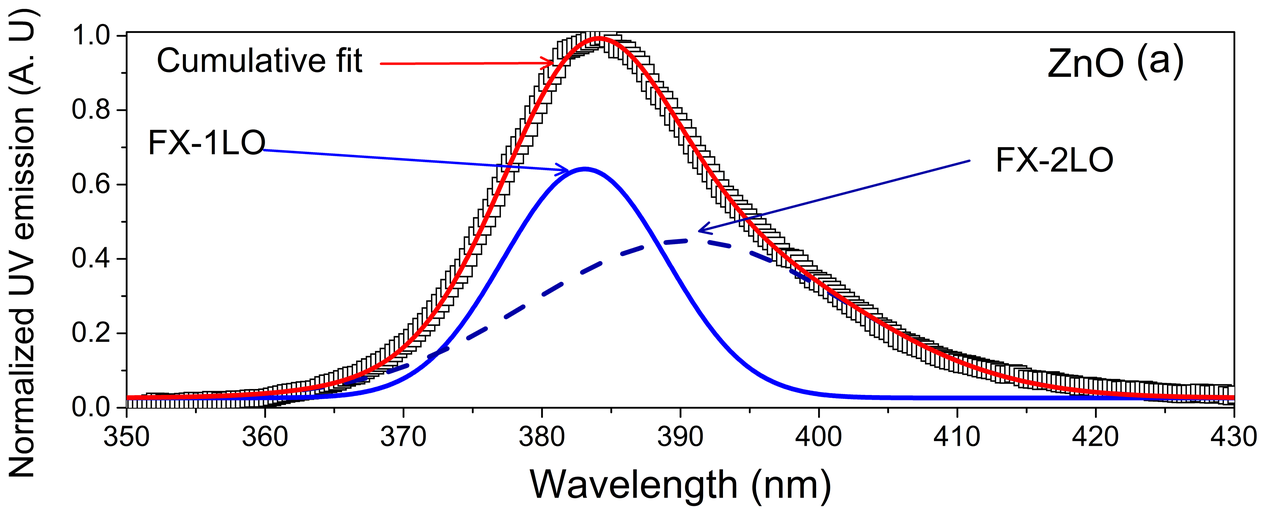
Cumulative fit
FX-1LO
FX-2LO
ZnO (a)
Normalized UV emission (A. U)
Wavelength (nm)

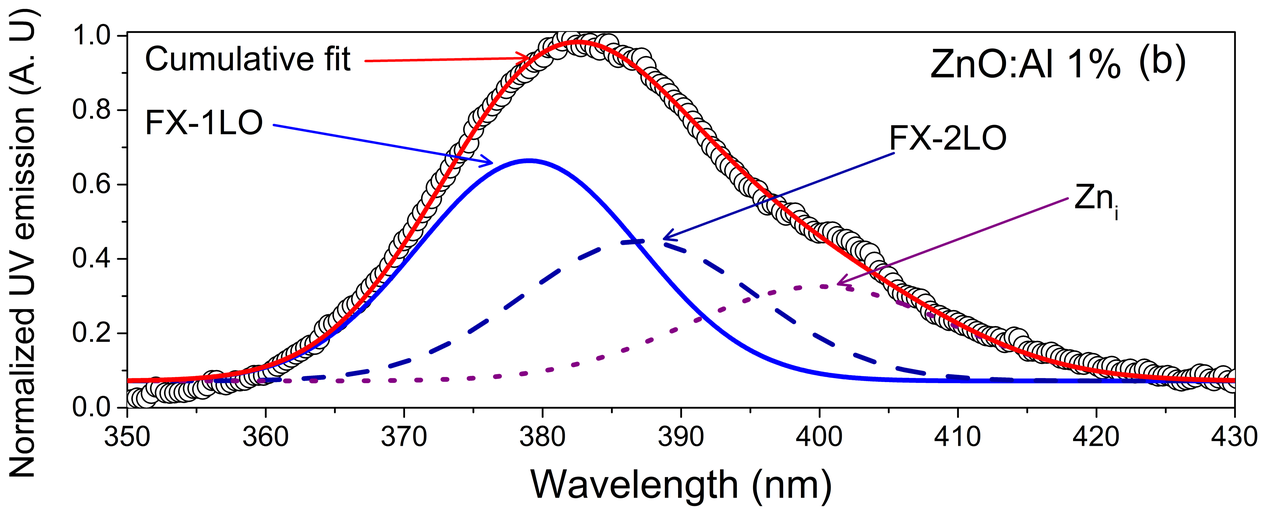
Cumulative fit
FX-1LO
FX-2LO
Zn$_i$
ZnO:Al 1% (b)
Normalized UV emission (A. U)
Wavelength (nm)

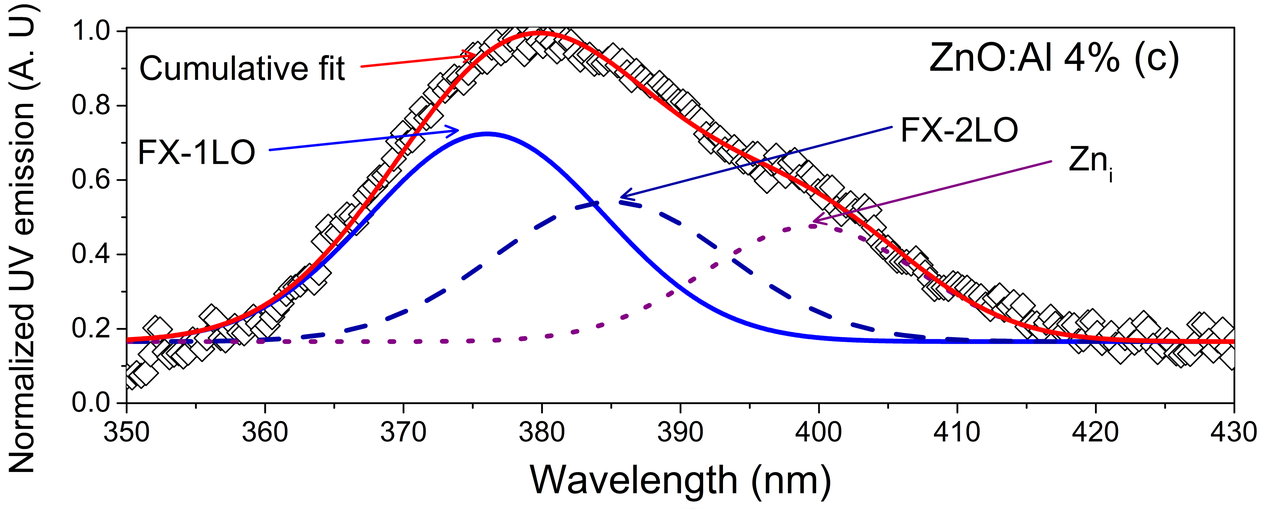
Cumulative fit
FX-1LO
FX-2LO
Zn$_i$
ZnO:Al 4% (c)
Normalized UV emission (A. U)
Wavelength (nm)

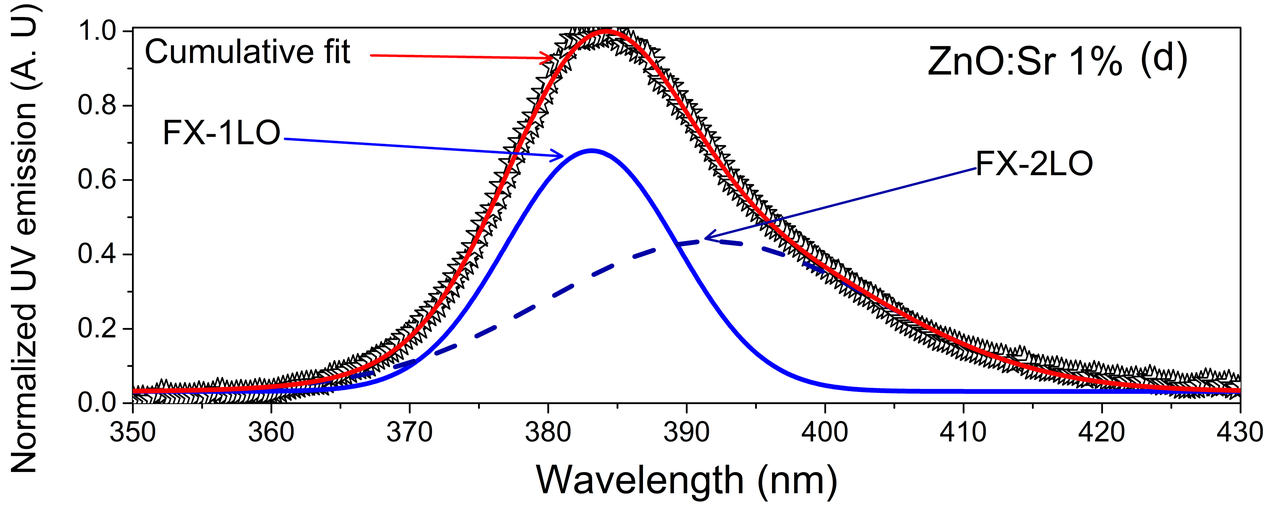
Cumulative fit
FX-1LO
FX-2LO
ZnO:Sr 1% (d)
Normalized UV emission (A. U)
Wavelength (nm)

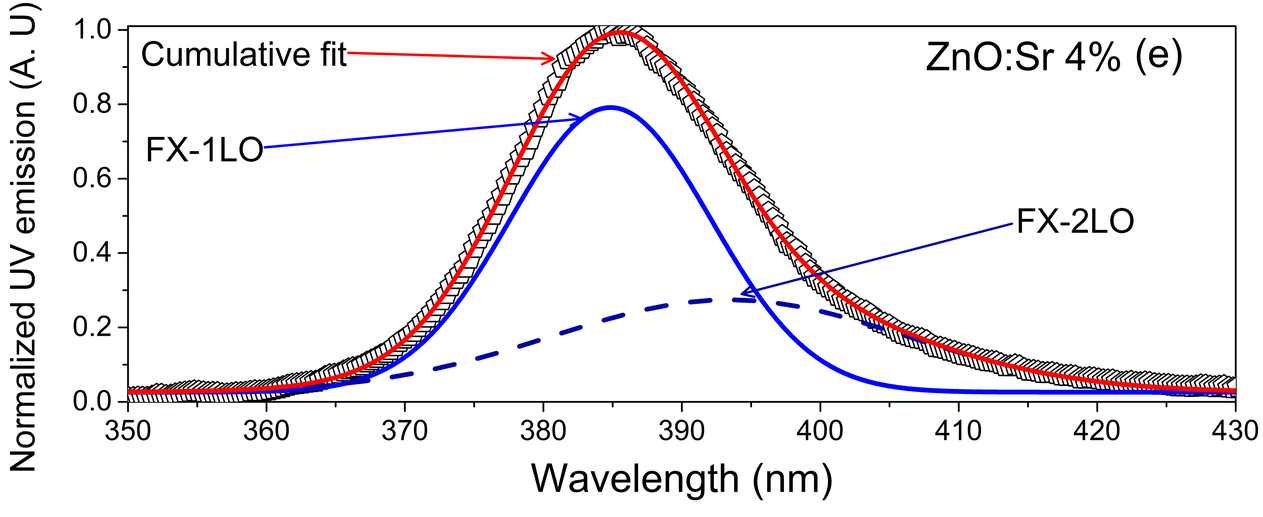
Cumulative fit
FX-1LO
FX-2LO
ZnO:Sr 4% (e)
Normalized UV emission (A. U)
Wavelength (nm)

Highligths

- ZnO and ZnO:M (M = Al^{3+} and Sr^{2+}) powders were synthetized by a hydrothermal method
- The particles radius decreased from 1 μm down to 70 nm with Al dopant incorporation
- Both Al^{3+} and Sr^{2+} are mainly incorporated substitutionally
- Al^{3+} and Sr^{2+} additions to ZnO induce compressive and tensile strain respectively
- Al^{3+} incorporation induced a PL component at ~3.1 eV related with Zn interstitial